Wollin, C., Bohnhoff, M., Martinez Garzon, P., Küperkoch, L., Raub, C. (2018): A unified earthquake catalogue for the Sea of Marmara Region, Turkey, based on automatized phase picking and travel-time inversion: seismotectonic implications. - *Tectonophysics*, *747-748*, pp. 416—444.

DOI: http://doi.org/10.1016/j.tecto.2018.05.020

A unified earthquake catalogue for the Sea of Marmara Region, Turkey, based on automatized phase picking and travel-time inversion: Seismotectonic implications*

Christopher Wollin[1], Marco Bohnhoff[1,2], Patricia Martínez-Garzón[1], and Ludger Küperkoch[3]

[1] *GFZ German Research Centre for Geosciences, Section 4.2 'Geomechanics and Rheology', 14473 Potsdam, Germany*
[2] *Free University Berlin, Department of Earth Sciences, 12249 Berlin, Germany*
[3] *Bestec GmbH, 76829 Landau, Germany*

August 24, 2018

*Published as a research article in Tectonophysics: Christopher Wollin, Marco Bohnhoff, Patricia Martínez-Garzón, Ludger Küperkoch, Christina Raub, A unified earthquake catalogue for the Sea of Marmara Region, Turkey, based on automatized phase picking and travel-time inversion: seismotectonic implications, *Tectonophysics*, 2018, ISSN 0040-1951, https://doi.org/10.1016/j.tecto.2018.05.020.

Abstract The Marmara section of the North Anatolian Fault Zone (NAFZ) is late in its seismic cycle and can be expected to produce a magnitude M up to 7.4 earthquake during the next decades in direct vicinity to the 15-million population center Istanbul. This setting translates the seismic hazard into very high risk and makes a thorough understanding of the current seismotectonic setting of this NAFZ section a pressing task. The absence of near-fault stations along most part of the offshore Marmara section limits the reliability of existing seismicity catalogues for this region. For the first time we combine the different regional permanent networks thereby optimizing azimuthal coverage and present a refined hypocenter catalogue for the Sea of Marmara on this basis. Compared to the original locations, adoption of a refined automated technique to determine precise onset times for the different body waves and an iterative travel-time inversion scheme, lead to substantial improvement of 6812 absolute earthquake locations, particularly in the epicentral distribution. The automated processing is explained in detail. Further optimization is achieved through relative relocation of 4407 earthquakes. Our catalogue covers more than a decade (2006 – 2016) with a regional moment-magnitude of completeness of Mc = 2.1. The epicentral distribution delineates the Marmara Section, i.e. the northern NAFZ branch, as the seismically most active fault strand. We identify several aseismic fault patches that are interpreted to represent locked parts of the fault. Seismic activity in the past decade predominantly occurs off the main fault on the edges of the aseismic patches, supporting previous studies that the Marmara section of the NAFZ contains both locked and creeping fault portions. Single-event focal mechanisms ($2.7 \leq \mathrm{Mw} \leq 4.5$) indicate that currently both strike-slip and normal faulting occur, confirming the transtensional setting of the region.

Keywords: catalog unification, phase picking, earthquake location, transform faults, seismotectonics, seismic hazard

Keypoints

1. Compilation of a new $10\frac{1}{2}$-year hypocenter catalogue for the Marmara region based on an optimized virtual seismic network
2. Employment of a novel automated waveform picking procedure as well as an iterative travel time inversion
3. Identification of seismically active and inactive fault patches along the offshore Marmara segment of the North Anatolian Fault Zone where a M7+ earthquake is overdue
4. Observation of coherent fault segments and local faulting regimes from high-precision relocated hypocenters and focal mechanisms

Contents

1. Introduction

Monitoring seismicity along active hazardous faults requires adequate seismic networks to reliably determine the spatial distribution of hypocenters, characterize the fault-zone geometry and subsequently discriminate active from inactive fault strands. Major onshore transform faults such as the San Andreas Fault in California, most parts of the North Anatolian Fault Zone (NAFZ) in Turkey, or the Dead Sea Transform in the Near East provide good pre-conditions for near-fault monitoring and subsequent hazard and risk estimates for nearby population centers such as e.g. the Los Angeles metropolitan region or the San Francisco bay area. In contrast, the Marmara section of the NAFZ in northwestern Turkey represents a ∼140 km long fault that runs offshore below the Sea of Marmara and it is thus inaccessible for onshore near-fault stations operating at low noise conditions along most of its part. The difficult access for permanent near-fault monitoring is also true for geodetic (GPS) campaigns.

There is wide consensus that the Marmara section of the NAFZ is late in its seismic cycle and can be expected to produce a magnitude M > 7 earthquake during the next decades, [e.g. Parsons, 2004, Murru et al., 2016, Bohnhoff et al., 2016b]. This seismic hazard translates into very high risk, because the fault is co-located with the Istanbul metropolitan region with its 15 or more million inhabitants. Consequently, one of the most pressing issues is to image the geometry of the offshore Marmara fault segments and determine their faulting regimes as a prerequisite to improve and optimize hazard and risk assessment for the region. To achieve this, a reliable hypocenter catalogue with lowest possible but regionally consistent magnitude of completeness is needed. However, due to the absence of near-fault stations along the most part of the Marmara section, this is a challenging task and can only be achieved through optimizing both, the azimuthal station coverage throughout the region and the picking accuracy for the arrival times of the different body waves.

In this paper, we present a unified hypocenter catalogue for the time period 2006–2016 combining for the first time the two major national permanent seismic networks of the region operated by the Disaster and Emergency Management Presidency of Turkey (AFAD) and the Kandilli Observatory and Earthquake Research Institute (KOERI), and also including near-fault recordings from the local PIRES (Princes' Islands Realtime Earthquake monitoring System) and GONAF (Geophysical Observatory at the North Anatolian Fault) networks in the eastern Sea of Marmara. The unified seismic network consists of a total of 83 landbased permanent seismic stations in the immediate vicinity of the Sea of Marmara region with full azimuthal coverage and locally unprecedented station density. The integrated data from the different seismic networks was consistently processed using a refined automated picking procedure developed and fine-tuned to determine arrival times of the P and S waves with the highest possible precision. The newly compiled homogeneous seismicity catalogue allows to define the individual fault strands of the NAFZ below the Sea of Marmara and their faulting kinematics from focal mechanism solutions. Based on refined relative hypocenter relocations, seismically active or quiet fault segments throughout the Marmara region are identified and discussed in the light of the pending M > 7 earthquake.

The paper is organized as follows. After introducing the tectonic setting of the North Anatolian Fault Zone in the Marmara region (Sec. 2), we describe the integrated data and our employed automatized processing scheme (Sec. 3). While the automatically determined picks can be considered intermediate results and we evaluate their quality at this point of methodical account, section 4, 'Results and Discussion', is dedicated to the description and interpretation of the new earthquake locations, magnitudes as well as focal mechanisms (which are based on the picks). We finally conclude on the insights gained by creating a unified and consistent earthquake catalogue (Sec. 5).

2. Tectonic setting of the North Anatolian Fault Zone in the Istanbul-Marmara region

The NAFZ is one of the largest plate-bounding transform faults on Earth and its regional seismotectonic setting was extensively studied since it was first reported in the late 1940s [Ketin, 1948]. The fault zone separates the Anatolian and Eurasian plates extending for some 1200 km between the Karliova triple junction in Eastern Anatolia and the Gulf of Saros Northern Aegean [e.g. Barka, 1992, Şengör et al., 2005, Bohnhoff et al., 2016b]. Westward movement of Anatolia has developed in the framework of the northward moving Arabian plate [Reilinger et al., 2006, Bulut et al., 2012]. It is also connected to the southward rollback of the Hellenic subduction zone, where the African lithosphere is subducted below the Aegean [Flerit et al., 2004, Bohnhoff et al., 2005]. The NAFZ generally exhibits a right-lateral strike-slip fault over most of its extent. Except for the Ganos bend [Janssen et al., 2009], no substantial thrust components have been identified from focal mechanisms of larger earthquakes during the 20th century. The average slip rate along the NAFZ as determined from GPS is 20–25 mm/yr with increasing values towards the west [Reilinger et al., 2006]. The pure strike-slip system along the bulk of the NAFZ east of the Sea of Marmara turns into a transtensional setting in NW Turkey due to the rollback of the Hellenic subduction zone that started a few million years ago and that resulted in the opening of the Sea of Marmara as a large pull-apart structure [Şengör et al., 2005, Le Pichon et al., 2015]. This transtensional system still evolves and is currently further progressing towards the east resulting in the younger and thus smaller pull-apart structures at the eastern tip of the Sea of Marmara (Cinarcik Basin) [Karabulut et al., 2002, Le Pichon et al., 2001, Acarel et al., 2014] and further onland along the 1999 Izmit rupture (Akyazi Plain) [Bohnhoff et al., 2006, Bulut et al., 2007, Najdahmadi et al., 2016].

The NAFZ forms a single main fault strand along most of its part from eastern Anatolia to the Bolu region. Approximately 150 km east of the city of Izmit the fault splits into two major branches known as the northern and southern NAFZ strands in northwestern Turkey [Le Pichon et al., 2014]. Most of the NAFZ deformation in northwestern Turkey occurs along the northern fault strand below the Sea of Marmara, here named 'Marmara Section' [Reilinger et al., 2006, Hergert and Heidbach, 2010, Ergintav et al., 2014] (Fig. 1).

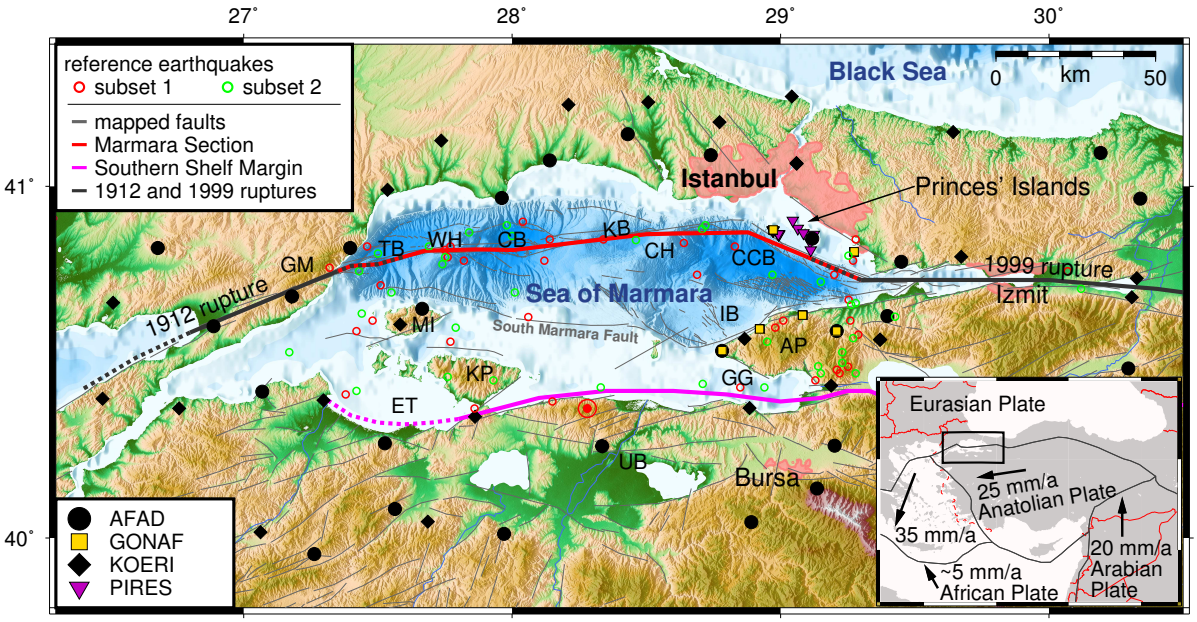

Figure 1: The North Anatolian Fault Zone (NAFZ) around the Sea of Marmara region. The 1912 Ganos and 1999 Izmit earthquake ruptures are indicated by the thick gray lines. The NAFZ is highlighted in red. The Southern Shelf Margin [Armijo et al., 1999, Murru et al., 2016] is delineated in magenta. Abbreviations in capital letters name some common topographic features: Tekirdağ Basin (TB), Western High (WH), Central Basin (CB), Central High (CH), Kumburgaz Basin (KB), Çınarcık Basin (CCB), Imrali Basin (NIB), Armutlu Peninsula (AP) all after Bécel et al. [2009], Gulf of Gemlik (GG), Kapıdağ Peninsula (KP), Erdek Tombolo (ET), Marmara Island (MI), Ganos Mountains (GM) all after Şengör et al. [2014], Uluabat Basin (UB) after Le Pichon et al. [2014]. Seismic stations of permanent seismic networks used in this study are indicated by different symbols. The bathymetry and submarine faults are after Le Pichon et al. [2001] and Armijo et al. [2005] and onshore faults are after the Turkey General Directorate of Mineral Research and Exploration (pers. comm.). Larger cities (Istanbul, Izmit, Bursa) are plotted as pink areas. Red and green circles mark the epicenters of two subsets of earthquakes for which onset times of crustal phases were manually determined (see Section 3.2.1 for details). The bold red circle located on the southern coastline marks the event whose waveform recordings are shown in Fig. 7. The inset in the lower right shows the area of study in the broader tectonic regime with respect to stable Eurasia.

In the historic past, the Marmara Section of the NAFZ created dominantly strike-slip but also M > 6 normal faulting earthquakes such as the 1963 earthquake below the eastern Sea of Marmara [Bulut et al., 2007]. The offshore Marmara section is bound by the two most recent magnitude M > 7 earthquakes of the region, the 1912 Mürefte-Ganos event in the west [Ambraseys, 1970, Janssen et al., 2009] and the 1999 Izmit and Düzce events in the east [Tibi et al., 2001, Pinar et al., 2001, Barka et al., 2002, Bohnhoff et al., 2016a] (Fig. 1). The Marmara Section last ruptured in 1766 with a M7.4 event. The estimated recurrence time for this event is 200–250 years [Parsons, 2004, Bohnhoff et al., 2016b] indicating that this fault is currently in the final phase of its seismic cycle and thus needs to be considered as a seismic gap posing a major threat to the Istanbul metropolitan region. The southern NAFZ strand hosts only 20 % of Anatolia's westward motion [e.g. Ergintav et al., 2014]. It is located in the southern Sea of Marmara shelf [Le Pichon et al., 2001, Armijo et al., 1999] and bypasses the Sea of Marmara to its south, south of the Uluabat Basins, bending SW thereafter before entering the Aegan Sea [Armijo et al., 1999, Le Pichon et al., 2014] (Fig. 1). It is of "fragmented" nature [Şengör et al., 1985, Le Pichon et al., 2003, 2014] and displays transtensional structures south of the Sea of Marmara. While there is consensus on the potential for a larger (M up to 7.4) event in this region, there is an ongoing discussion on the dominant type of faulting to be expected. The two end-members discussed in the literature are the activation of a single through-going strike-slip fault (the so-called "Main Marmara Fault") [Le Pichon et al., 1999, 2001] versus the activation of several smaller en-echelon normal faults [Armijo et al., 2002, 2005]. While the "Main Marmara Fault" model predicts a single strike-slip event with a larger magnitude of up to 7.4 and subsequent implications for intense ground-shaking, the normal faulting events would probably not exceed M∼7 but host the potential for local tsunamis. Pinar et al. [2003] summarized several other models for a variety of fault systems in the Sea of Marmara including the two above-mentioned end-members. The authors themselves proposed that the main fault between the two most recent major ruptures in 1912 and 1999, should be decomposed into three throughgoing right-lateral subsegments which are linked by right and left stepovers and numerous subsidiary faults.

Between the northern and southern NAFZ branches, two other secondary fault strands have been identified. The first of these follows the southern coast of the Sea of Marmara coinciding with the "Southern Shelf Margin" [Armijo et al., 1999] and it was named the "Central North Anatolian Fault" by Murru et al. [2016] (Fig. 1). Faults in this structure have been mostly attributed to normal faulting-type seismicity [Le Pichon et al., 2001]. Additionally, Le Pichon et al. [2014] delineated a deformation zone between Marmara Island and the Armutlu Peninsula (Fig. 1) named the "South Marmara Fault". This structure strikes WNW forming a wide arc bypassing Marmara Island and then continuing further westward sub-parallel to the Ganos fault. The fault was characterized as right-lateral strike-slip and the end of its activity was dated to 5 Ma ago when motion of the Anatolian plate started to be predominantly accommodated by the northern branch [Le Pichon et al., 2014].

3. An improved seismicity catalogue for the Marmara region in the years 2006–2016

Due to the geologic setting of the Marmara region, with the largest portion of the Marmara Section being located below the seafloor between 10 and 30 km offshore the northern and up to 50 km away from the southern coast, permanent or long-term high-precision seismic monitoring is mostly constrained to the deployment of land-based seismometers at substantial distance to the fault. This generally limits the resolution capability, especially for precisely determining the absolute hypocentral depth and subsequently also for accurate single-event focal mechanisms due to the absence of near-fault stations. Deploying ocean-bottom seismometers to densely sample the entire focal sphere is an alternative approach, but their long-term operation remains a difficult task and signal quality is usually limited due to coupling issues and enhanced noise levels on the seafloor [Sato et al., 2004, Bulut et al., 2009, Schmittbuhl et al., 2015, Yamamoto et al., 2017]. The only near-fault on-land spots are located in the eastern Sea of Marmara, where the Princes' Islands and selected onshore spots were recently equipped with permanent stations including surface and downhole vertical arrays [Bulut et al., 2009, 2011, Bohnhoff et al., 2013, 2017a,b].

Consequently, the best way to achieve a homogeneous seismicity catalogue in this region is as follows: (1) optimizing the azimuthal station coverage by combining stations from the different permanent regional networks; (2) reducing location uncertainties by applying optimized identification and timing of P- and S-wave arrival times; and (3) applying strict quality criteria and station corrections prior to traveltime inversion for hypocenter determination in the absence of a high-resolution 3-D velocity model. Point (2) includes a unified processing of seismic waveforms aiming at assuring consistency among the arrival times.

3.1. A unified Marmara seismic network

On the land surrounding the Sea of Marmara, two regional permanent seismic networks are in operation. The Disaster and Emergency Management Presidency of Turkey (AFAD) and the Kandilli Observatory and Earthquake Research Institute (KOERI) operate two extensive but separate permanent networks of seismic stations throughout Turkey with higher station density in the broader Marmara region. For the first time, waveform recordings from both national networks were here combined to a single virtual regional seismic network with unprecedented station coverage along the entire Marmara section of the NAFZ (Fig. 1). We focused our study on the time period spanning from beginning of 2006 to mid-2016 thus comprising almost 10 $\frac{1}{2}$ years. We also included near-fault recordings from the PIRES network and the GONAF borehole observatory which started operation in 2006 and 2015, respectively [Bulut et al., 2009, 2011, Bohnhoff et al., 2013, Prevedel et al., 2015, Raub et al., 2016, Bohnhoff et al., 2017a] (Fig. 1). Incorporating further waveform data from additional temporary seismological deployments such as short-term local land-based networks or individual ocean bottom seismometers

can only increase catalogue precision for a limited sub-region and time period. Thus, it does not substantially contribute to a regionally decreased magnitude of completeness for the entire Marmara region and the entire time period considered here.

The bulk of seismic recordings used in this study were provided by KOERI, from which we selected a total of 39 stations. Between 2006 and 2013, most KOERI waveform recordings were sampled with 50 Hz. After 2013, the sampling rate was doubled to 100 Hz. From AFAD, digital recordings were available from 29 stations from 2009 onwards. Their waveform data was consistently sampled at 100 Hz. Furthermore, the recordings from 16 PIRES stations were sampled at 200 Hz covering the entire considered time period between 2006 and 2016. Lastly, GONAF recordings from six boreholes sampled at 500 Hz were available from 2015 onwards. All station locations are shown in (Fig. 1).

We based our study on the seismicity catalogues provided by KOERI, AFAD and PIRES, which were merged into a single catalogue containing event origin time and hypocentral coordinates. Locations of the different catalogues were calculated on the basis of different velocity models. Whereas KOERI and PIRES use velocity models derived for the eastern Sea of Marmara [Karabulut et al., 2002, Bulut et al., 2009, , respectively], AFAD locations are determined with one standard velocity model throughout Turkey. The individual catalogues provide different magnitude scales (predominantly durational and local magnitudes). We also compared the resulting list of events with the seismicity catalogue provided by MARsite (`www.marsite.eu`) to ensure that no event located anywhere along the entire Marmara section of the NAFZ during the considered period of time was missing. Duplicated earthquakes were removed, by applying a density based clustering analysis to the origin times [DBSCAN, Ester et al., 1996]. Clusters of origin times were defined for pairs separated by less than 30 s. By keeping all earthquakes with unclustered origin times and the earliest occurrence within clusters, we obtained a total number of 12,186 events.

3.2. Manual and automated timing (picking) of seismic phases

We analyzed ∼580,000 three-component recordings (47 per event on average) from all 86 available stations for the entire 10-year time period where the waveforms were cut to a time interval of 240 s (1 min before to 3 min after the origin time given in the merged catalogues) thereby ensuring to include full body wave trains and their coda even for stations up to ∼200 km epicentral distance. In total we retrieve ∼360,000 P- and S-picks. The here applied automatic picking procedure, i.e. the procedure for timing P- and S-wave onsets, is essential for the derived quality of the hypocenter catalogue and therefore the applied methodology is described in detail below. The automatic picking procedure primarily serves the purpose to ensure consistency among the seismic arrival times which are the most important intermediate results for a study of regional seismicity as done here. This is relevant because otherwise, the consistency of phase data acquired from independently operating data centers or researchers cannot be presumed.

Figure 2: Stacked frequency distributions of moment-magnitudes of two sets of reference events that were manually picked.

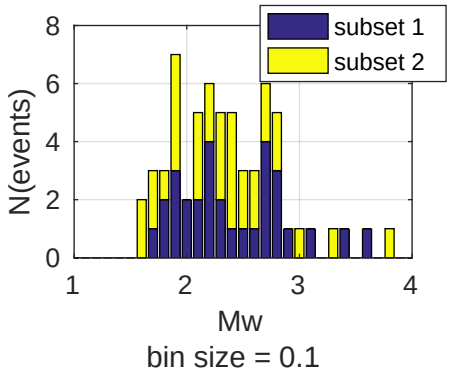

3.2.1. Manual reference picking

In order to evaluate and optimize the automatically derived P- and S-wave arrival times, we first defined two subsets of seismic events from the entire hypocenter catalogue. All waveforms for both subsets were then consistently manually picked (P and S). Each subset consisted of 36 events. In order to achieve an even spatial distribution of events throughout the target area (the entire Marmara region), we subdivide it into a regular mesh of rectangles. We then randomly sample the events in each individual cell without replacement. The number of events drawn per cell is a discrete function of the total count of events in a cell. The function is defined such that relatively few are drawn from cells with many events, thus dampening the probabilistic weight of eventclusters. Accordingly, to even out the more frequent occurrence of small events described by the Gutenberg-Richter distribution, large magnitudes were given an increased probabilistic weight, i.e. the probability for an event to be drawn as function of its magnitude remains constant at $\sim$0.05% until a magnitude threshold at $M_{thresh} = 2.6$ and increases linearly from there onwards with $\sim$3 percentage points per magnitude until a maximum magnitude of $M_{max} = 5$. The events making up the two subsets are marked in Fig. 1 (red and green circles, respectively) and the magnitude frequency distribution of those later successfully located is shown in Fig. 2.

Manual reference picking was done following the strict criteria of Diehl et al. [2009], identifying an earliest and latest possible, as well as the most likely phase onset time for three different crustal P phases (Pg, Pn, PmP) and their S pendants. We also measure the first-motion polarity of all P-phases if possible. The different crustal P phases were defined after [Shearer, 1999]: Pg denotes the direct P-wave bottoming within the crust. Pn-waves bottom in the uppermost mantle and, being refracted at the Moho, are the first arriving phase at epicentral distances beyond the crossover point at 80–120 km distance. Lastly, PmP denotes P-reflections at the Moho. Note, that this definition differs slightly from the one given in the IASPEI standard nomenclature of seismic phases [Bormann et al., 2013] which differentiates between upper and lower crust [Storchak et al., 2003]. Around the cross-over point, the Pn and Pg phases may not be

identified unambiguously. In this case, phases were labeled in the order of their arrival, e.g. a phase which arrives certainly first but which is of unknown type will be labeled P1. Phase onsets whose placing in the order of arrival could not be established with certainty were simply labeled with P as proposed by Diehl et al. [2009]. Using previous catalogue locations, the horizontal recordings were transformed from vertical/north/east to vertical/radial/transverse coordinates prior to reference picking.

In order to identify the different crustal phases we calculated their travel time branches with a 1-D ray tracer using two different P-wave velocity models. Bulut et al. [2009] provide an optimized 1-D velocity model for the eastern Sea of Marmara which is roughly congruent with the corresponding sections of an east-west trending wide-angle seismic profile across the Sea of Marmara [Bécel et al., 2009]. The latter study though, reveals a significant crustal thinning along the North Marmara Trough stretching along 40°45' N from 27°30' E to 29°E. In the west, the crustal thickness of more than 30 km sharply decreases to 26 km. Although not resolved with high accuracy, Bécel et al. [2009] describe a crustal plateau of the same thickness that stretches 120 km between the western and eastern edges of the North Marmara Trough. We adopted this shallow crust in our second velocity model. For each earthquake, P- and S-wave arrival times of the above-mentioned crustal phases were estimated by plotting a travel-time section based on the event locations of the initial hypocenter catalogue, and travel time branches calculated for both 1-D velocity models. The task of manual reference picking was then accomplished with the 'Picking and Location Tool' (PILOT), a MATLAB® based software developed by [Küperkoch, 2011]. Here the operant is supported by automatically adapting a time and amplitude window according to the given noise level, thus implementing the suggestions for consistent reference picking given in Diehl et al. [2009].

The manual picks of the first subset served as a reference to finetune the automatic picking procedure (also see the end of the next section). Once the algorithm reproduced the manual picks to a satisfactory degree, its performance was independently compared to and evaluated with the second subset. With this procedure we ensured the highest possible picking precision for the automatic picker. An exemplary direct comparison of reference and automatic picks on the three component recordings of an individual station is displayed in Fig. 6. Reference picks for a multitude of vertical channels recording one seismic event are shown in a seismic section (Fig. 7). A quantitative evaluation of the automatic algorithm's performance with respect to the joint subsets of reference picks is discussed further below in Section 3.2.3.

3.2.2. Automated picking

The algorithm to automatically determine P and S wave onset times is based on the approach of Küperkoch et al. [2010, 2012] who use a two-step procedure during which a preliminary and a final pick are set using a narrow and a wider causal band-pass filter in order to first effectively suppress noise and then include the relevant frequency band, respectively. For the preliminary and final P-pick (S-pick) we used a 3rd order Butterworth band-pass filter with cut-off-frequencies of [2, 12] Hz and [1, 33] Hz, respectively ([2, 12] Hz and [1, 16] Hz), where the upper cut-off frequency was adapted to 75 % of

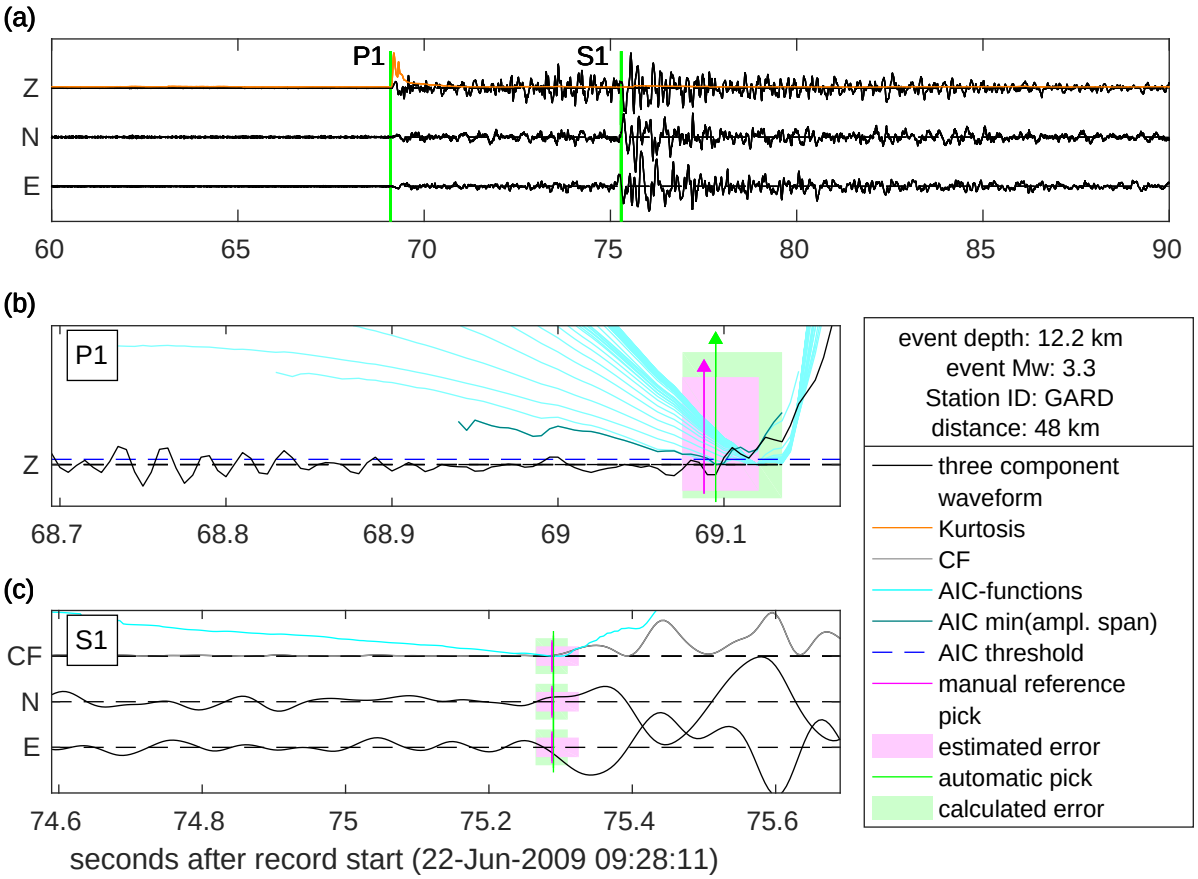

Figure 6: (a) Exemplary 3-component recording with kurtosis (orange line) of the vertical recording and automatic first arrival P- and S-picks (P1 and S1 in green). (b)+(c) Zoom-in of the P- and S-pick, respectively, together with the corresponding manual reference picks (in magenta). Pale rectangles depict the interval of uncertainty of the respective pick. (b) Also indicates the manually and automatically determined first-motion polarity of both reference and automatic picks as well as the suit of AIC functions used to automatically determine the P-onset and to calculate its uncertainty. (c) Horizontal components and their characteristic function (CF). The suit of AIC functions used to derive the S-pick and its uncertainty is similar to the one shown in (b) and is subsumed into one representative AIC function for better overview here (also see legend).

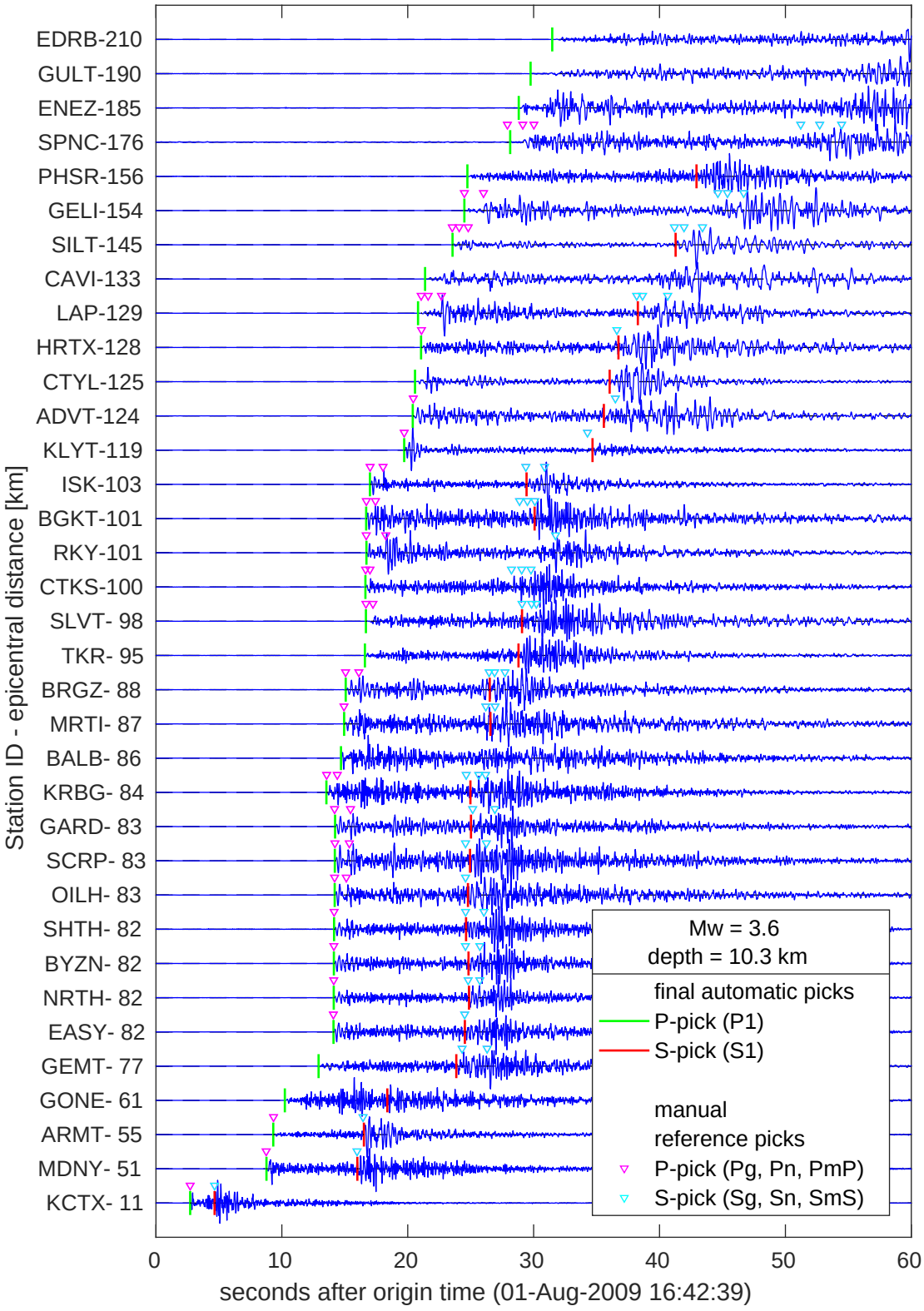

Figure 7: (Caption is on the next side.)

Figure 7: Vertical component recordings of a Mw = 3.6 earthquake located in the southern central Sea of Marmara (see Fig. 1 for location) plotted with the traces sorted by epicentral distance. Green and red markers indicate automatically derived P- and S-wave onset picks, respectively. Magenta and cyan colored triangles show manually picked arrival times of different crustal P- and S-phases respectively.

the Nyquist frequency for 50 Hz recordings. We additionally defined asymmetric pick uncertainties similarly as during the reference picking, by calculating the earliest and latest possible times bounding the uncertainty for every automatically determined phase onset.

While keeping the two-step approach of Küperkoch et al. [2010, 2012], we here refined the inner procedure by using Higher Order Statistics (HOS, Eq. 1) as a refined trigger to crudely estimate the P-phase onset (e.g. as applied in Ross and Ben-Zion [2014]). The timely development of the HOS kurtosis, causally calculated on a 2 s long moving window, and its maximum (crudely indicating the beginning of the wave train) are illustrated in Fig. 4. Furthermore, the Akaike Information Criterion (AIC) [Akaike, 1974] in Maeda's representation (Eq. 2) [Maeda, 1985] was repeatedly applied to different wavelet portions containing the phase onset with high certainty in order to pick it as accurately as possible and also to calculate left- and right-sided bounds for the uncertainty. The AIC-function after Maeda is a time series that ideally yields a global minimum at the time of the signal onset. However, the precise point in time containing the global minimum is very sensitive to the actual wavelet window transformed with the AIC-function. We thus systematically calculated suits of AIC-functions on moving and nested windows of the waveform and used the variability of the global minima to estimate an asymmetric uncertainty for the pick. A moving window of 20 s length splitting the waveform into 100 overlapping portions was used to calculate the preliminary, and 100 nested windows to calculate the final pick. In order to obtain a meaningful minimum for each AIC-function it was important, that each window of the underlying time-series contained noise and a portion of the seismic signal. The moving windows always contained the maximum of the kurtosis with an overlap of 1 s. The largest of the nested windows was 10 s long and all contained the uncertainty interval of the preliminary pick. Fig. 5 shows a closeup of the vertical recording in Fig. 4 around the P-pick. Each AIC-function has a global minimum and the earliest of all is defined as the most likely onset. The pick's uncertainty was then defined as the time domain within which the suit of AIC-functions remains below a certain threshold. This threshold was individually defined for every pick. Out of all members of the corresponding suit of AIC-functions we chose that with the smallest span of amplitudes (dark cyan in Fig. 5) and define the threshold as twenty and ten percent of its largest deflection (dashed blue horizontal line in Fig. 5) for the preliminary and final pick, respectively. The earliest and latest possible times for the phase onset were then defined as the left- and right-sided bounds of the pick's uncertainty.

The P-wave uncertainty assessment described above was developed in order to capture

not only the uncertainty inherent by the shape of the onset, i.e. emergent or impulsive, and the signal-to-noise ratio (SNR), but also the frequent scenario of close sequential phases, e.g. a head- followed by a direct wave close to the crossover point (see the Section 3.2.1) where, the first phase onset may be closely succeeded by a more prominent one. In such a case, the targeted first onset is often mistaken for the more prominent one, not only by the original automatic algorithm [Küperkoch et al., 2010] but also in manual phase readings [Diehl et al., 2009]. Usually the automatic algorithm can be tuned to pick the correct onset on an individual trace, yet with dramatic consequences for the accurate processing of other traces. Our approach is designed to assign larger uncertainties in these doubtful cases, possibly spanning a time interval containing both onsets.

A similar two-step procedure and a suit of AIC-functions are also used to calculate the S-picks and their bounds of the uncertainty. Here we followed [Grigoli et al., 2014] and calculated the timely development of the largest eigenvalue of the instantaneous covariance matrix [Vidale, 1986] (uppermost row in Fig. 6) of both horizontal waveform components (E- and N-components in Fig. 6). This time series served as a characteristic function (CF) and was then used to calculate the suit of AIC-functions.

The picking process was interrupted and the corresponding pick discarded under the following circumstances: (a) the trace had smeared energy, i.e. the timely distribution of energy peaks in the 4 min long waveform was not concentrated on a bounded domain as characteristic for a well recorded earthquake, (b) the P-pick was too early or too late, i.e. occurring at a point in time that belongs to a different event or an epicenter outside the network, (c) the P-wave had a lower SNR on the vertical component than on the horizontal components (indicating that the P-pick has likely been set in front of a S-wave onset), (d) P- or S-pick had SNR below 1, or (e) the S-pick SNR was too low. We used the automatic algorithm described above to analyze ∼580,000 three-component recordings from 12,186 earthquakes, this way retrieving ∼360,000 P- or S-picks in total. Figure 7 shows automatic P- and S-picks on top of the vertical waveforms of a seismic event (Mw = 3.6) recorded throughout the unified seismic network. The manual reference picks are shown for comparison.

In order to determine focal mechanisms for the best covered and located events, in addition to the onset times the first-motion polarities of P-waves were also determined automatically. After applying the same band-pass filter as for the final P-pick to the vertical recording, we measured the slope of two straights both crossing the first local extremum after the pick. The first straight also intersects the amplitude at the picked P-wave onset whereas the second intersects the first local extremum before that point in time. The first motion was declared to be positive or negative, if both straights had positive or negative slope, the ratio of maximum signal to maximum noise level was larger than 4, and the standard deviation of noise and signal was larger than 3, where the waveform interval of [-1.00, -0.05]s and [0.05, 0.30]s before and after the P-pick were considered to represent noise and signal, respectively.

For the tuning of the algorithm the interplay of the band-pass filters and the windowing of the seismograms was important. We chose a narrow band-pass filter first, to reduce noise as much as necessary in order to obtain characteristic onsets of the kurtosis. The width of the second filter was increased to display details of the phase onset as for

instance the first-motion polarity. The width of the wavelet windows as base for the suits of AIC-functions as well as their overlap with a characteristic point in time (the maximum of the kurtosis and the maximum of the CF for the P- and S-pick, respectively) was also adopted to the regional seismicity observed. The AIC-threshold was chosen larger for the preliminary pick, thus creating a sufficiently large timely interval for the search of the final pick.

3.2.3. Assessment of reference versus automated picks

We performed a quantitative comparison of manually derived reference picks of the different crustal phases and the automatically calculated P- and S-phase onsets by calculating their time difference (Fig. 12). The picking residual for the primary phase (P-wave) is thus defined as $\Delta t = t_A(P1) - t_m(\tilde{P})$ where $t_A(P1)$ represents the automatically determined pick and $t_m(\tilde{P})$ several manually derived reference phase onsets of different crustal phases as defined above (Section 3.2.1), namely $\tilde{P} \in \{Pn, Pg, PmP , P1, P\}$. As such Δt is negative/positive if the automatic pick is earlier/later than the designated reference pick. $\Delta t = t_A(S1) - t_m(\tilde{S})$ is defined equivalently and the distribution of Δt is shown for the combined subsets of reference events for the P- and S-phases in Fig. 9 and Fig. 10, respectively.

The automatic algorithm was designed to pick the first arriving phase only. Therefore, the distributions for the automatic picking residual to $\tilde{P} = Pg$ and $\tilde{P} = Pn$ (green and magenta graphs in Fig. 9 and 10), whose order of arrival depends on the epicentral distance, consider reference picks only if they are first to arrive. The residual distribution obtained from stacking the distributions for the reference phases Pg, Pn, P1 and P (i.e. all first arriving P- and S-phases expected to correspond to the automatic P1- and S1-pick) peaks at zero time difference and contains 68 % of all values within ∼0.1 s. The equivalent distribution for the S-phases peaks at 0.02 s and contains 68 % of all values within ∼0.3 s. Fig. 9 and Fig. 10 also show the residual distributions to the reflected crustal phases PmP and SmP. They only count negative values indicating that, as expected, the automatic algorithm always picked earlier on the corresponding trace.

Figure 11 and Fig. 12 show two-dimensional histograms comparing the uncertainty assigned during the reference picking (x-axis) and that calculated by our algorithm (y-axis) for P- and S-picks respectively, where the picking uncertainty is defined as the domain of uncertainty, i.e. the time difference between latest and earliest possible pick $dt = t_l - t_e$ (see Section 3.2.1 and Section 3.2.2). Diagonal elements represent cases where automatic and reference uncertainty lie in the same range.

Over 35 % of uncertainties assigned during the reference picking of P-wave onsets lie in the range between 0.025 and 0.125 s (i.e. in the histogram bins of 0.05 s and 0.10 s) and have a corresponding automatic pick in the same uncertainty range (Fig. 11). Increased occurrences above the diagonal at reference uncertainties larger or equal to 0.15 s indicate that the statistical uncertainty estimation performed by our algorithm undermatches the reference uncertainties in this interval. The spread of calculated S-pick uncertainties is much larger than that of the P-picks (Fig. 12). Most reference uncertainties lie in the histogram bins between 0.05 s and 0.35 s and a large fraction is paired with slightly

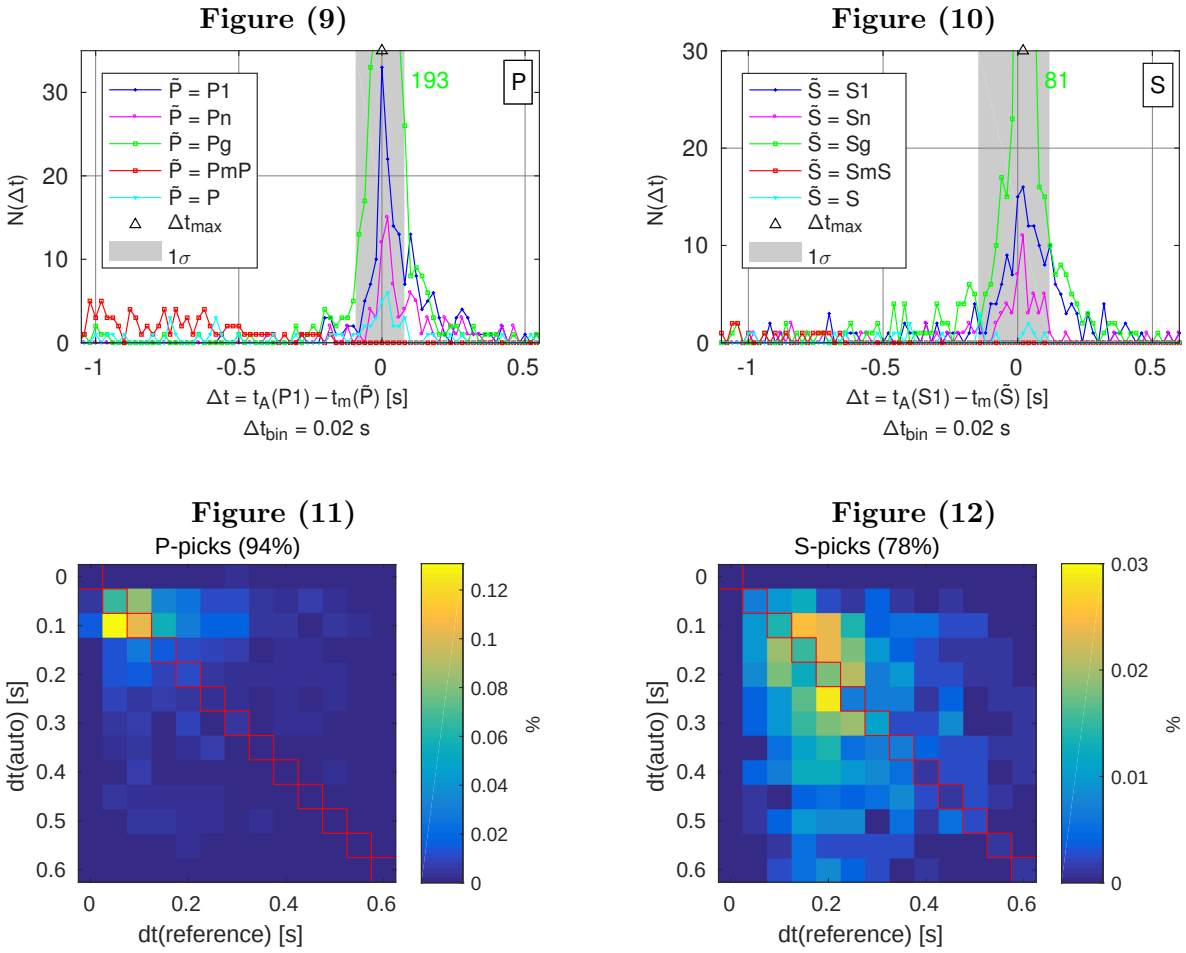

Figure 12: Residual Δt between automatic and manual reference picks with respect to different crustal phases associated to (a) a P- and (b) a S-wave (see Section 3.2.1 for detailed explanation, e.g. of individual ray paths of different crustal phases). 68 % of pick residuals (1σ neighborhood) lie within the area shaded in darker gray (including all first arriving phases). Two-dimensional histograms in (c) and (d) display how well the picking uncertainties calculated by our algorithm, dt(auto), match those assigned during the reference picking, dt(reference), by counting occurrences of pairs of values. Each square has a width of 0.05 s. The percentage in the title expresses the fraction of uncertainty pairs with both uncertainty values below 0.6 s.

lower calculated uncertainties. However, the automatic algorithm also returns a tail of larger uncertainties. The discrepancy can be explained with the different approaches for determining the pick uncertainties: on the one hand the deterministic approach described by Diehl et al. [2009] is still subjected to the consistent performance of the human operator, whereas the algorithm relies on a multitude of statistically derived picks repeatedly applying the AIC. Overall the distributions of P- and S-pick uncertainties calculated with our algorithm peak at smaller values and have a long tail of large values.

We also compare automatically calculated with manually derived first-motion polarities. Fig. 41 displays the fraction of manually derived Up- and Down first-motions that were determined with the same or opposite polarity or were left undetermined by the automatic algorithm. In this way we can estimate that on average, out of all reference Up- and Down-first-motions 90 % were determined correctly.

3.3. Hypocenter determination

With ∼360,000 automatically determined P- and S-wave arrival times (P- and S-picks) we perform a travel-time inversion using the HYPOSAT software [Schweitzer, 2001] that is based on Geiger's stepwise linearized least-squares method [Geiger, 1912]. We tested the performance of different 1-D velocity models and selected the model from Karabulut et al. [2011] that was developed for the broader Sea of Marmara region. We selected this particular model due to the best trade-off between number of relocated events and depth accuracy. We then calculated station corrections in order to account for a systematic delay or acceleration of phase arrival times due to heterogeneities of the wave propagation velocity in the rock volume in the immediate vicinity of a seismic station. For this purpose, we first inverted for the hypocenter of every earthquake using picks with the smallest uncertainties (P-picks were included if they belonged to the lower 66-percentile of an event's P-pick uncertainty distribution or if they belonged to the 95-percentile and had a S-pick, which was then also included in the inversion). At this point HYPOSAT performed two subsequent inversions, where the depth was kept constant during the first and was then retrieved after the second inversion. The correction for the P- and S-phase arrival times at a station was then obtained from the mean of the travel time residual distribution of all preliminary locations at this particular station. The succeeding inversions performed to obtain the final locations, used travel times from which the corresponding station corrections were subtracted.

In order to identify and discard imprecise picks and at the same time retain as much travel-time information as possible, we implemented an iterative inversion scheme similar to Sippl et al. [2013] which tests the results of many inversion runs obtained with different sets of picks. The high number of possible combinations of picks associated with an earthquake prevents the rigorous testing of all such combinations, and the presented work-flow is a compromise to computational expense. The earthquake location methodology applied here was as follows:

1. In a first step, we calculated the standard deviation of $y = t_A(S) - \mathrm{sqrt}(3) * t_A(P)$ for pairs of automatic P- and corresponding S-picks, $t_A(P)$ and $t_A(S)$ respectively,

assuming $v_P/v_S \approx \sqrt{3}$. We then preliminarily excluded S-picks for which y is beyond the 1σ neighborhood.

2. For the initial inversion of this iterative procedure the remaining picks from 1) were subjected to the same selection as used during the calculation of station corrections. Here and in the subsequent steps, travel times were directly inverted for a hypocenter location until otherwise stated (in contrast to HYPOSAT's optional procedure to perform two inversions keeping depth constant during the first and retrieving it after the second, the direct inversion for the hypocenter is computationally much faster).

3. Successively removing picks with travel time residuals exceeding two times the travel time RMS (tt-RMS), the inversion was repeated while the tt-RMS of the new location dropped below 2/3 of the value of the previous run or a minimum of four P-picks was reached.

4. In order to regain as much information about the event as possible we re-tested all picks discarded in the previously described steps 1)–3). The picks to be tested were sorted according to the epicentral distance of the associated station, quality (smallest uncertainty margin) and phase. Beginning with the best P-phase of the nearest station, the picks were individually added to the set of picks previously inverted and kept only if the added pick's residual did not exceed 2.5 times the new location's tt-RMS and the latter did not exceed 1.2 times the tt-RMS of the result of the last inversion run yielding an improvement, where the last location obtained in step 3) was used as initial reference.

5. The set of picks obtained after step 4) was considered best and the location constrained by choosing HYPOSAT to invert for the epicenter with fixed depth before inverting for the depth as well (this is the default behavior of HYPOSAT and also yields the best locations when a consistent set of picks is provided). If the results deviated significantly from the location obtained after step 4) the inversion was considered unstable. In this case we attempted to obtain a better constraint on the epicenter by repeating steps 2)–4) with the hypocentral depth fixed at 10 km. Doing so, the inversion did not yield any estimate for the depth uncertainty.

6. Finally, we checked the consistency of depth and depth uncertainty. If the event was located with zero depth, or the upper bound for the depth's uncertainty exceeds the surface level or no depth uncertainty was retrieved, we inverted the most suitable set of picks obtained from step 4) with fixed depth, where different values for the depth were probed. We began with depths from 0 to 30 km in a 5 km spacing. The subsequent loop probed the depth interval around the depth of the location with the lowest RMS value in a 1 km spacing. This procedure was repeated until reaching a spacing of 0.1 km and the final location was chosen by the lowest RMS value.

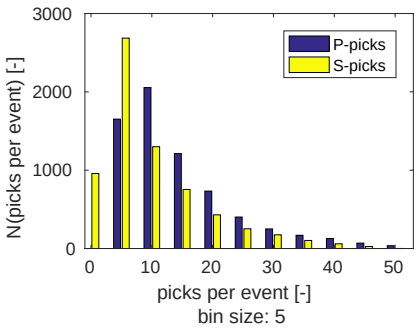

Figure 13: Frequency of events located with a certain number of P- and S-picks (the two distributions must be read separately from one another, e.g. the majority of events were located with 8-12 P-picks and $\approx$ 1000 with 0-3 S-picks). Events falling under the category of best, good or fair locations are considered (see Table 1). The bins are centered around multiples of five.

The parameters presented in 1)–4) were found by optimizing earthquake locations achieved with a number of observations larger than average but at the same time resulting in large location uncertainties in terms of tt-RMS and error ellipse area. With this procedure we determined a total of 11,835 absolute hypocenters out of the 12,816 events for which P- and S-onset times were picked. Table 1 shows how categories of best, good and fair event locations can be obtained by imposing limits to the minimum number of total, P- or S-picks as well as maximum values for the azimuthal gap and horizontal uncertainty (expressed by the error ellipse area), where the sets of locations are nested with increasing strictness of the selection criteria, e.g. the set of good locations is a subset of the set of fair locations. Out of 6812 fair locations 5098 were retrieved after step 5) of the iterative inversion scheme, 1714 after step 6). For these locations a total of $\sim$98,600 P- and $\sim$65,700 S-picks have finally been inverted. Figure 13 displays the frequency of fair locations with a certain number of P- and S-picks and Fig. 14 the travel-time residual RMS distributions by quality. Approximately 2000 of the fair locations are characterized by RMS-values smaller than 0.2 s, thus underestimating location-uncertainty and indicating that more phase-arrival observations would be needed to realistically constrain it. Fig. 15 displays histograms of the horizontal uncertainties in terms of the error ellipse area and vertical location errors in km^2 and km (blue graph in the main plot and yellow in the inset), respectively. The abundant occurrence of vanishing vertical uncertainties smaller than 1 km affects locations of all qualities and is clearly too optimistic. We obtain a more realistic estimation after refining the hypocenters with a relative relocation procedure described in the following section. The epicenters of this subset of well located events are shown in Fig. 17 and discussed in the corresponding Section 4.1.

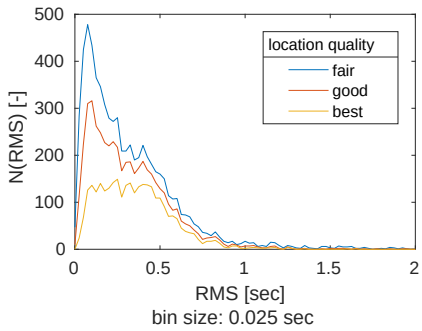

Figure 14: Travel time RMS distribution of absolute locations by location quality (see Table 1).

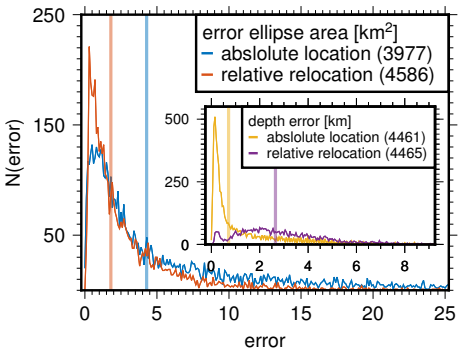

Figure 15: Frequency distributions of horizontal uncertainty in terms of the error ellipse area in km^2 and depth uncertainty in km (inset) of relative relocations and corresponding absolute locations, where the histogram bin-size is $0.5\,km^2$ (km). The median of each distribution is indicated by thick vertical lines in the corresponding color and the number in brackets behind the legend entries equals the sum of all data points shown.

3.4. Double-difference relocation of hypocenters

In order to further refine the relative precision of hypocenters we relocated the catalogue of absolute locations employing the double-difference technique [Waldhauser and Ellsworth, 2000]. We computed for each earthquake differential travel times of up to six neighboring events with a maximum separation of 20 km and based our relocation procedure on the P- and S-wave automatic picks. In the first iterations of the relocation procedure, all differential travel times were considered, and the differential travel times from S waves were given half of the weight of the corresponding differential travel times from the P waves. In the following iterations, we constrained the residual threshold gradually up to 0.5 s as well as the maximum distance between linked pairs gradually down to 6 km. After the relocation procedure, we obtained 4657 refined hypocentral locations. We further produced suits of 100 locations for every event by repeating the relocation procedure 100 times, perturbing the set of differential travel times according to their distribution obtained at individual stations. The hypocentral uncertainty was then assessed for individual events where the distribution of the corresponding locations defined error-ellipsoids containing 68 % of solutions [Waldhauser and Ellsworth, 2000]. Table 3 lists how the very best locations can be obtained upon imposing limits to the extent of the error ellipse. A refined regional catalogue of 4407 high-precision hypocenters is further analyzed and discussed (Fig. 18). The according distribution of the horizontal and vertical uncertainties is summarized in Fig. 15 (red graph in the main plot and purple graph in the inset, respectively). Compared to the absolute locations, particularly large horizontal uncertainties have been improved. The distribution of the vertical uncertainties of our final locations has a global maximum at 2.0 km and a mean value of ∼3.8 km.

3.5. Calculation of Moment Magnitudes

In order to unify the magnitude scale of the examined earthquakes, moment magnitudes were determined following a procedure that was recently applied to data sets from the eastern Sea of Marmara and Izmit/Düzce regions [Raub et al., 2017]. The method relies on using J and K integrals over the squared velocity and displacement spectra, respectively, as first introduced by Andrews [1986] and Snoke [1987]. Here, the spectra were calculated for waveform portions of vertical components around the P- as well as of horizontal components around the S-wave onset. Corrections for instrument response, spectral bandwidth and attenuation were applied in the frequency domain, and the low-frequency spectral level, needed for calculating the seismic moment, was estimated from the J and K integrals (Eq. 10 in Snoke [1987]). The moment magnitude was finally derived from the seismic moment using the relationship given by Hanks and Kanamori [1979]. For details on the magnitude determination we refer to Raub et al. [2017]. P- and S-wave velocities at the source were determined using the 1-D velocity model also used during the travel time inversion [Karabulut et al., 2011]. We estimated the earthquake's magnitude as the mean of all moment magnitudes retrieved from the individual traces of all three-component recordings associated with an event. We only excluded

Table 1: Different employed quality classifications and resulting number of absolute event locations $N_{locations}$, based on the following criteria: minimum number of picks (N_{min}), minimum number of P- and S-picks ($N_{P,min}$ and $N_{S,min}$, respectively) , maximum area of the ellipse representing the horizontal location uncertainty ($A_{errEll,max}$).

	Quality	$N_{locations}$	GAP_{max}	N_{min}	$N_{P,min}$	$N_{S,min}$	$A_{errEll,max}$
1	best	3054	180°	0	10	5	36km^2
2	good	4937	200°	0	4	3	64km^2
3	fair	6812	270°	7	0	0	256km^2
4	all	11835	360°	0	0	0	inf km^2

waveform recordings with a signal-to-noise ratio smaller than 10, measured around the corresponding phase onset and within the used bandwidth for the magnitude determination. Results for the calculation of 5353 moment magnitudes are further discussed in the following section.

4. Results and discussion

4.1. Absolute epicentral and magnitude distribution

The iterative localization scheme described in the previous section yields 11,835 absolute hypocenter locations of varying location quality. Thus we applied strict quality criteria to only select events with highly reliable locations for further interpretation (Table 1). Figure 17 depicts the epicentral distribution together with individual error ellipses of the catalogue of absolute earthquake locations subsumed under the category of fair locations for which events had to be located with at least seven picks, an azimuthal gap smaller than 270° and an error ellipse area of less than 256 km^2.

For locations categorized as fair, magnitudes were calculated as described in the previous Section 3.5. The magnitude range of the catalogue extends between $Mw_{min} = 0.7$ and $Mw_{max} = 4.5$ the variance of the individual network-magnitudes being smaller than 0.2 for all of the earthquakes. We used the goodness of fit method [Wiemer and Wyss, 2000] as described by Raub et al. [2017] to calculate the magnitude of completeness M_c. The b-value was calculated on the basis of the maximum likelihood method [Page, 1968]. Both methods were applied to the catalogue of fair absolute locations after removing events which were located shallower than 5 km and within areas that most likely contain quarry-blasts (green patches in Fig. 17). These areas were defined by the joined 4 km neighborhoods of quarry-blasts, intersected with land. The quarry-blast locations were taken from a separate catalogue provided by KOERI (see Fig. 18 for the according www-link). M_c and b-value were calculated for the remaining events, 1) for stricter catalogue qualities ('good' and 'best') and 2) for events located in the (entire) 'Marmara Region' as well as in sub-regions that correspond to the areas further investigated in cross-sectional volumes in the following section, namely the 'Marmara Section', 'Southern Shelf', 'Princes Island-' as well as 'Yalova-Hersek-Segment' and the Western Sea

Figure (17)

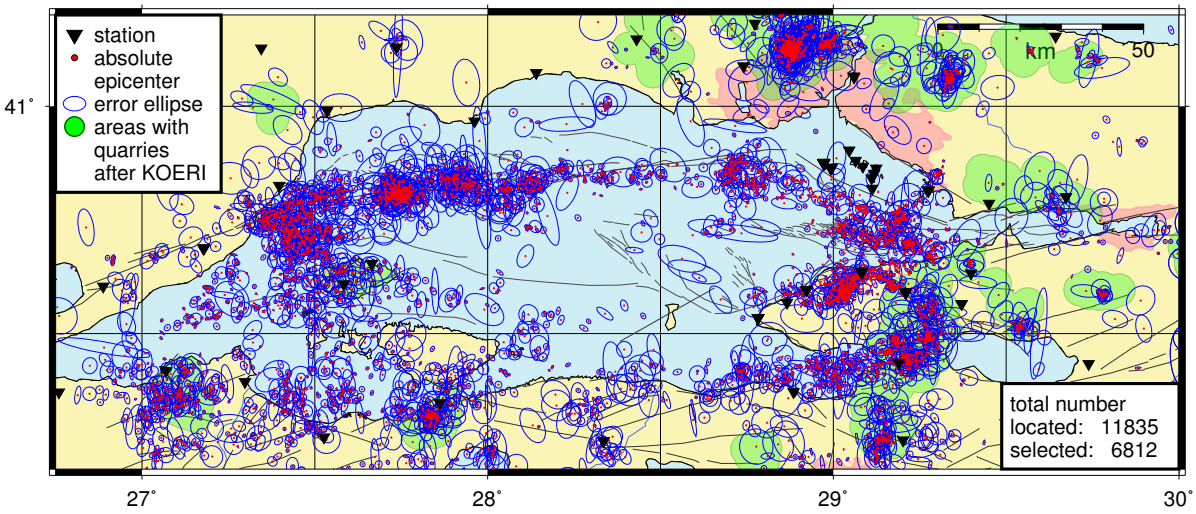

Figure (18)

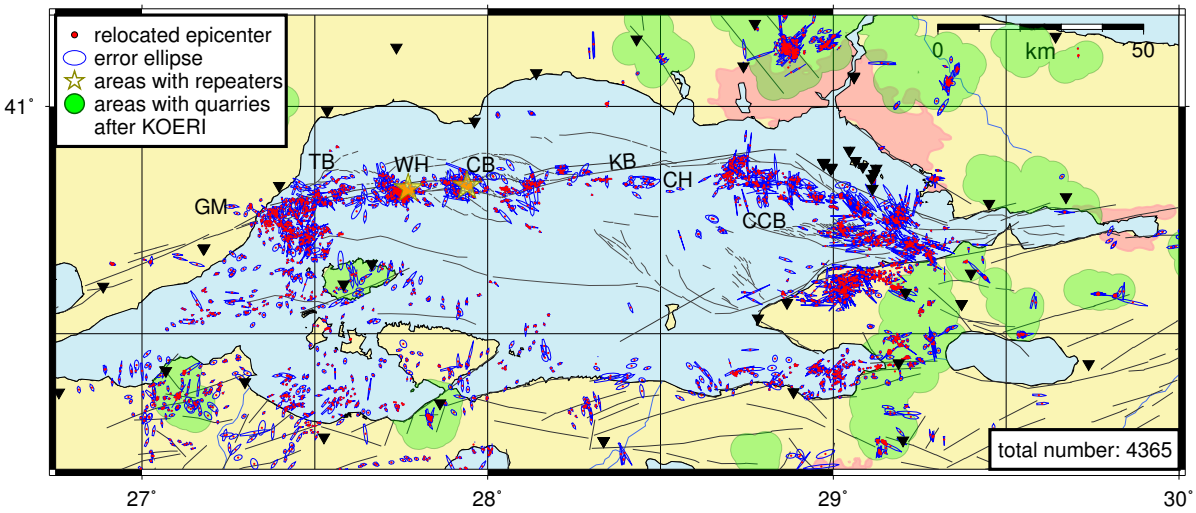

Figure 18: (a) Epicentral distribution of absolute locations for the broader Sea of Marmara region derived based on the automatic picks from the virtual network of 86 stations surrounding the Marmara Section of the NAFZ. A total of 6812 out of 11,835 located events of "Fair" quality (see Table 1 for specific constrains) were selected here. Epicenters are plotted with their lateral error ellipses. (b) Relative relocated epicenters of good quality (see Table 3) after applying the hypoDD double-difference technique [Waldhauser and Ellsworth, 2000] to the events from (a) resulting in a total number of 4407 events. The location of repeating earthquakes detected by Bohnhoff et al. [2017b] are marked with yellow stars. Regional abbreviations are like in Fig. 1. Areas colored in green contain quarry blasts as cataloged by KOERI (`http://www.koeri.boun.edu.tr/sismo/zeqdb/indexeng.asp`, last visited 2016.10.13). Dense epicentral clusters in the catalogue of relocated events within these areas and having relatively shallow depth are likely to be quarries (small green patches in Fig. 27 – 33).

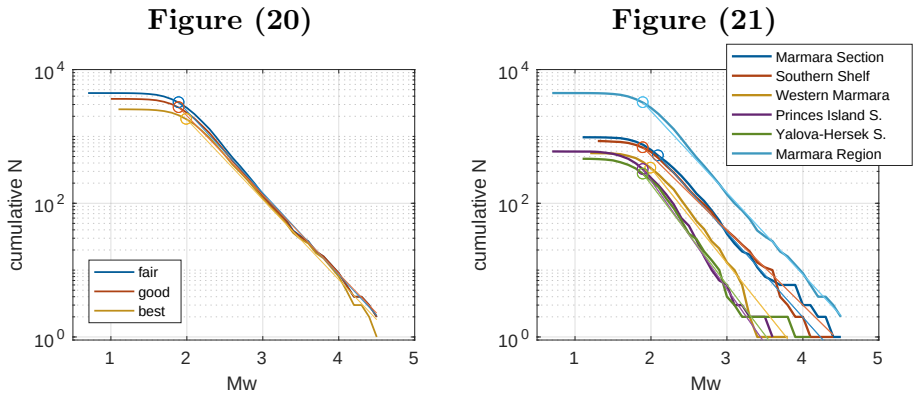

Figure 21: Cumulative magnitude-frequency distributions of absolute locations (Fig. 17), (a) for different catalogue qualities (Table 3) and (b) for different subregions. Shallow earthquakes inside areas likely containing quarries are not considered. The magnitude of completeness M_c and the b-value were obtained after bootstrap re-sampling and are marked by a circle and the slope of the straight, respectively. The numeric values of each are given in Table 2 together with references to maps showing the corresponding area.

of Marmara (Fig. 21). For each subset of magnitudes we performed a bootstrap re-sampling by repeating the calculation of Mc and b-value 1000 times on the basis of 75 % of the underlying magnitude population which was randomly sampled without replacement. The corresponding averages and standard deviations are summarized in Table 2 where M_c varies between 1.9 calculated for several subregions and 2.1 for the Marmara Section. This can be expected as the PIRES-network provides near-fault coverage while the Marmara Section is more distant to seismic stations. We obtain a reasonable b-value of $b = 1.24 \pm 0.05$ for the entire region and time period. Significantly larger b-values were measured for the Western Marmara (1.38) as well as for the Princes-Island- (1.59) and Yalova-Hersek-Segement (1.50). For the latter this could be related to a lower differential stress in that area, implying a normal fault regime, which is confirmed by the according focal mechanisms [Sec. 4.4, Fig. 34, Örgülü, 2011, Öztürk et al., 2015, Kinscher et al., 2013]. We can follow this line of argument for the Princes-Island-Segment by considering the two normal faulting events we here observe at its western tip (events 6 and 7 in Fig. 34. On the other hand, elevated b-values are also associated with areas of geological complexity and the activation of abundant small faults [Raub et al., 2017], such that the Princes-Island-Segment as described by Pinar et al. [2003] and the Western-Marmara containing the Ganos-Bend, could be such candidates.

Events contained in the categories of best, good or fair locations roughly constitute half of the events initially analyzed. The remaining events were not located with sufficient precision and thus discarded from further processing and analysis. Fig. 20 indicates how application of stricter quality criteria discards particularly events with $Mw < 2.1$. Small events are likely to be recorded properly only by a local subset of the seismic stations, thus yielding too few picks to retrieve a stable hypocenter.

Table 2: Summary of magnitude frequency-statistics of absolute locations as illustrated by Fig. 20 and 21 for different catalogue qualities and subregions, respectively, obtained after bootstrap re-sampling. The subregions are those investigated in Sec. 4.2.

region		quality	N(events)	M_c	b-value	
Marmara Section	(Fig. 27a)	fair	971	2.1 ± 0.1	1.29 ± 0.08	Fig. 21
Southern Shelf	(Fig. 27b)		853	2.0 ± 0.2	1.18 ± 0.09	
Western Marmara	(Fig. 33)		563	2.0 ± 0.1	1.39 ± 0.10	
Princes Island S.	(Fig. 29b)		596	1.9 ± 0.1	1.59 ± 0.10	
Yalova-Hersek S.	(Fig. 29d)		463	1.9 ± 0.1	1.49 ± 0.11	
Marmara Region	(Fig. 18)		4452	1.9 ± 0.1	1.25 ± 0.05	
Marmara Region	Fig. 17	fair	4452	1.9 ± 0.1	1.24 ± 0.05	Fig. 20
		good	3643	1.9 ± 0.1	1.23 ± 0.06	
		best	2544	2.0 ± 0.1	1.20 ± 0.02	

Comparison of old and new absolute locations The new locations achieve an improvement with respect to the initial hypocenters particularly in their horizontal distribution which shows less epicentral spread and sharper contours of seismically active clusters (Fig. 23). The new distribution also creates more differentiated hypocentral depths (Fig. 23a–23b). Several of the initial hypocenters seem to have been located at fixed depth (at 7.5 km), a substantial portion being distributed in a narrow band around this depth and another in a more diffuse manner at greater depth. In contrast, the bulk of new hypocenters are generally located deeper than 7.5 km which is likely related to the fact that the velocity model used in this study [Karabulut et al., 2011] is faster on average than that used for instance for the KOERI-locations [Karabulut et al., 2002]. Some seismicity, however, has been moved closer to the surface. Yet, differences in this behavior can be observed along the lateral extension of the two exemplary cross-sections. For instance at the Ganos bend which is situated offshore but near several coast lines, the seismic cloud delineates an EW dipping trend of the activity (from approximately 8 to 12 km) with some sparse events slipping to shallower depths. Further East, along the Marmara-Section around the Western-High (WH), near surface events seem to form systematic clusters of seismic activity. Depth accuracy, however, for shallow seismicity offshore is hampered by the here present sedimentary layers which are insufficiently reflected in the 1D-velocity model [Karabulut et al., 2011]. Near surface seismicity can also be observed at onshore segments of the southern cross-section where it is likely to represent query blasts. These observations are discussed in further detail together with the corresponding relative relocations in the following section. Because some of the features discussed are obscured in Fig. 23 by the catalogue plotted second and the dislocation vectors, we provide the two shown sets of hypocenters separately in a flip-book like manner in the appendix (Fig. 43–45).

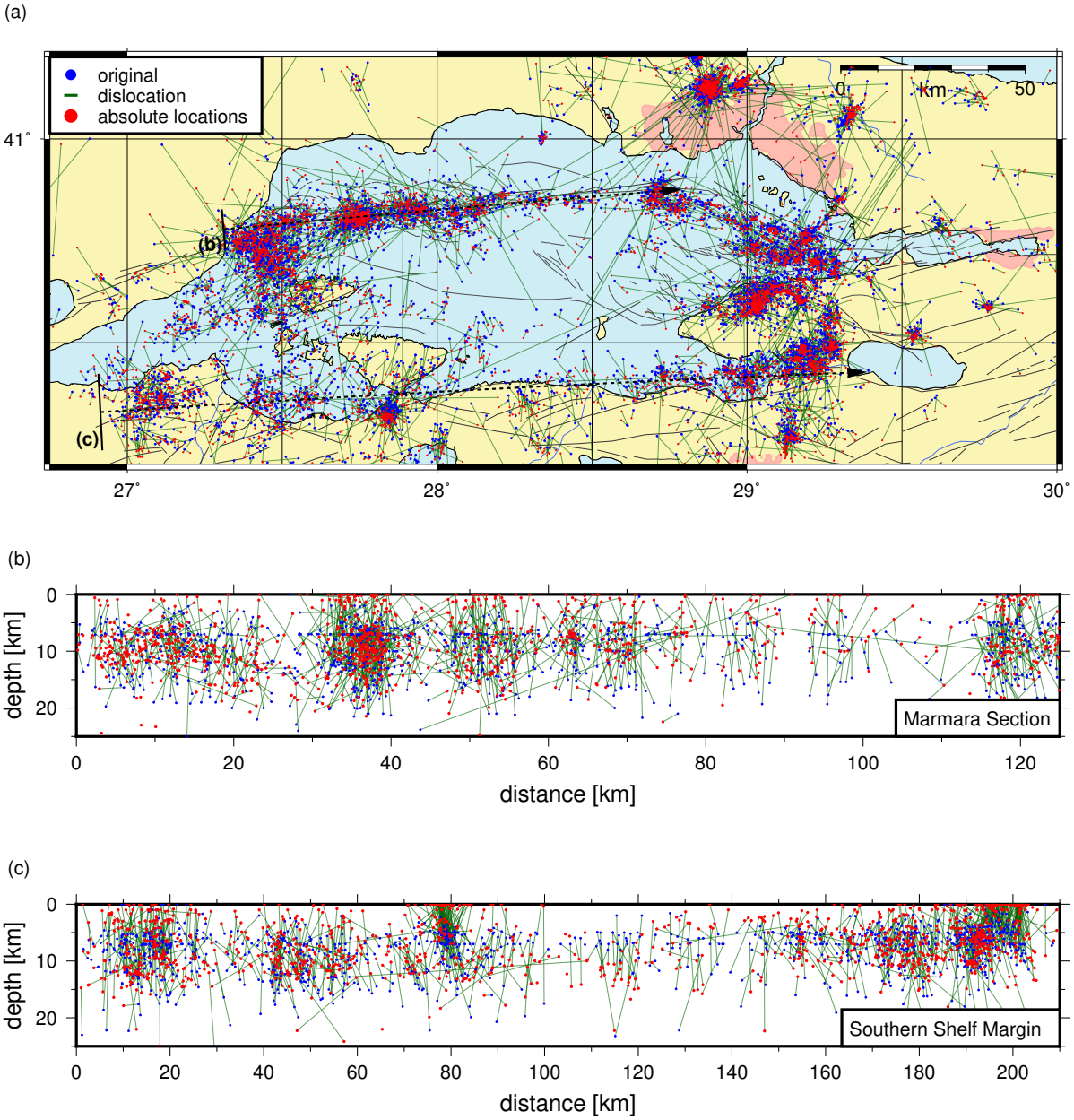

Figure 23: Dislocation (green lines) of fair absolute locations (red dots) as calculated in this study, from the original locations of the merged catalogues (blue dots) in (a) map view and in cross sections along (b) the Marmara Section and (c) the Southern Shelf Margin. The comparison of both catalogues is also provided as flip-book in the appendix where the two sets of hypocenters are plotted separately (Fig. 43–45).

Table 3: Different employed quality classifications and resulting number of relative relocations $N_{locations}$, based on the following criteria: maximum length of the error ellipse's major axis ($r_{major,max}$) and maximum area of the ellipse representing the horizontal location uncertainty ($A_{errEll,max}$).

	Quality	$N_{locations}$	$r_{major,max}$	$A_{errEll,max}$
1	very best	4407	9km	25 km^2
2	all	4657	inf km	inf km^2

4.2. Spatial distribution of relocated hypocenters

The here presented seismicity catalogue of relative relocated earthquakes consists of 4774 events throughout the Marmara region covering the time interval 2006–2016. We consider 4407 events with small horizontal location uncertainty for further analysis, i.e. maximum extent of major axis of error ellipse $\leq$ 9 km and maximum error ellipse area $\leq$ 25 km^2 (Fig. 18). Within the catalogue of the best relative relocations, we identify events which likely constitute clusters of quarry blasts. These clusters were defined by means of a density based clustering analysis [DBSCAN Ester et al., 1996], where a quarry-cluster had to consist of at least three events within 800 m epicentral distance and its centroid had to be situated in one of the areas previously constructed on the bases of the quarry-blast catalogue provided by KOERI (Fig. 18). The green shaded areas shown in Figures 27 – 33 were finally obtained by joining the 1.2 km neighborhoods of events that were members of the obtained clusters. Generally events within these areas are characterized by shallow hypocentral location, presumed as quarry blasts and discarded from further discussion.

Comparison of absolutely and relatively (re-)located hypocenters With respect to the absolute locations, the relative relocations achieve further compaction and sharpening of seismic clusters in the horizontal (Fig. 25). This is equally true for the vertical distribution although with less precision as compared to the horizontal. Nevertheless trends of the seismic cloud as well as sharp contours of some sub-clusters within it become visible (Fig. 25b–c). Generally, since the relative relocation initially relies on pairs of nearby seismicity, isolated seismic events are often discarded by the procedure. This mostly affects areas far from the core activity spots like for instance the water area in the middle of the Sea of Marmara. We further discuss the initial, absolute and relative (re-) locations in selected areas in the following paragraphs. The two sets of hypocenters shown in Fig. 25 are also provided separately in a flip-book like manner as electronic supplement in order to make visible features otherwise obscured by the dislocation vectors and the second layer of hypocenters (Fig. 47–49).

Central Marmara Section and Southern Marmara Shelf The majority of events are aligned offshore along the northern Marmara Section, extending between the Ganos fault in the west and the Central Basin in the east, and further eastward offshore of Istanbul

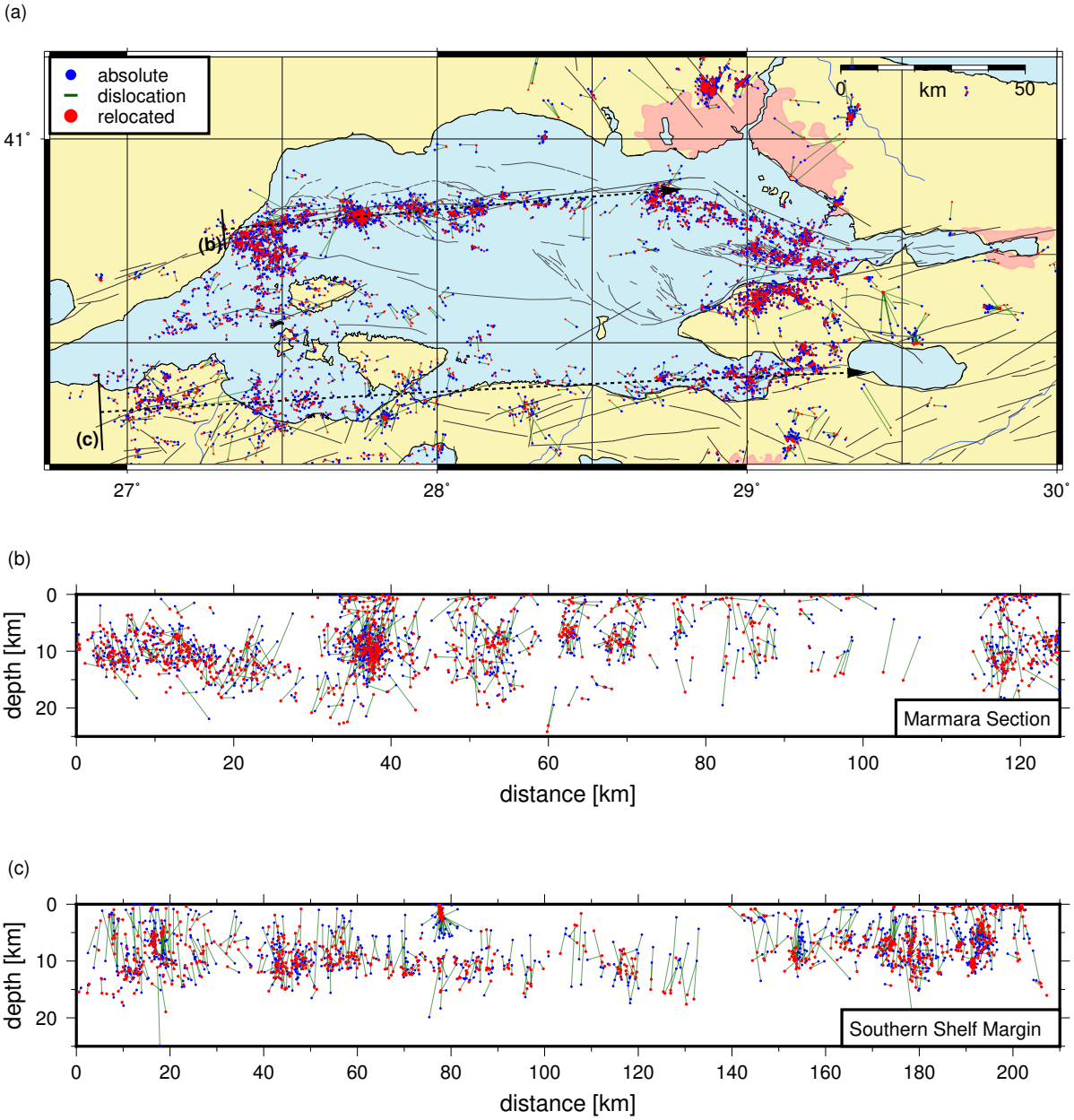

Figure 25: Dislocation (green lines) of relative relocations (red dots) from absolute locations (blue dots) in (a) map view and in cross sections along (b) the Marmara Section and (c) the Southern Shelf Margin. The comparison of both catalogues is also provided as flip-book in the appendix where the two sets of hypocenters are plotted separately (Fig. 47–49).

along the Princes' Islands segment and a fault aligned parallel to the northern coast of the Armutlu Pensinsula and running towards the Imrali Basin, the Yalova-Hersek segment [Pinar et al., 2001, Figures 1 and 27]. The Marmara Section as the seismically most active strand is part of the main northern NAFZ branch and hosts the largest part of the relative plate motion, on the order of 10–15 mm/yr [Hergert and Heidbach, 2010, Ergintav et al., 2014]. In first order approximation its trajectory through the Sea of Marmara is composed of succeeding straight segments delineated by coherent seismic activity and interrupted by several seismically less active – or entirely inactive – portions or spots. We refer to this later in the text. The width of the seismicity band is a few tens of kilometers on average with local variations. Whereas the transform fault character of the NAFZ suggests that the Marmara Section is a near-vertical fault, the verticality of the fault would imply that a substantial part of the activity is occurring off the main branch on secondary and/or splay faults. Such features have been observed earlier along the Princes' Islands segment with bursts of activity migrating along a splay fault [Bulut et al., 2011]. The second coherent seismically active feature seen in the epicentral distribution is pronounced activity along the Southern Marmara Shelf representing the northern part of the southern NAFZ branch (Figs. 1 and 27). There, the activity level is lower and events are less spatially clustered compared to the Marmara Section in the north.

The hypocentral depth of the seismicity generally extends from a few kilometers down to 16–18 km throughout the Marmara region. The depth distribution along the Marmara Section allows to identify systematic lateral variations of the hypocentral distribution (Fig. 27a). We highlight the trend of the lower bound of the seismogenic layer with an upper and lower estimate of the same, by calculating the depth down to which 85 – 95 % of the seismicity occurs in lengthwise equally long intervals. We applied this procedure to all cross sections (Figures 27 – 33), where the number of intervals a cross-section was divided into, was chosen such that every interval contained at least one event. The resulting values were locally averaged with a running mean. The activity spots west of the Tekirdak Basin (TB) and below the Western High (WH) show activity down to the base of the seismogenic layer (∼18 km) (Fig. 27a). The here reported depths are generally consistent with previous values reported by Schmittbuhl et al. [2015]. Only slight discrepancies can be observed in comparison with Yamamoto et al. [2017], who determine deeper hypocenters and vanishing shallow seismicity below the Western High (WH) using ten months of OBS data recorded immediately above the seismicity. Seismicity clusters and quiescent areas marked by Yamamoto et al. [2017] can also be identified in our catalog, indicating that there are no short-term spatio-temporal variations existing in the study area during the 10 years of observation except in shallow sedimentary layers where gas emissions have been reported [Tary et al., 2011] and seismicity there has been identified as after shocks to $M > 4$ earthquakes [Cros and Geli, 2013]. We find a similar trend of the lower boundary for the depth of seismic activity as Yamamoto et al. [2017] It becomes shallower towards the east, starting from a minimum of ∼18 km depth below the Western High, and passing the Central Basin (CB), it reaches down to ∼12 km only below the Kumburgaz Basin (KB) (Fig. 27a). In contrast, hypocentral depths east of the Central High drop to almost 20 km again (Fig.

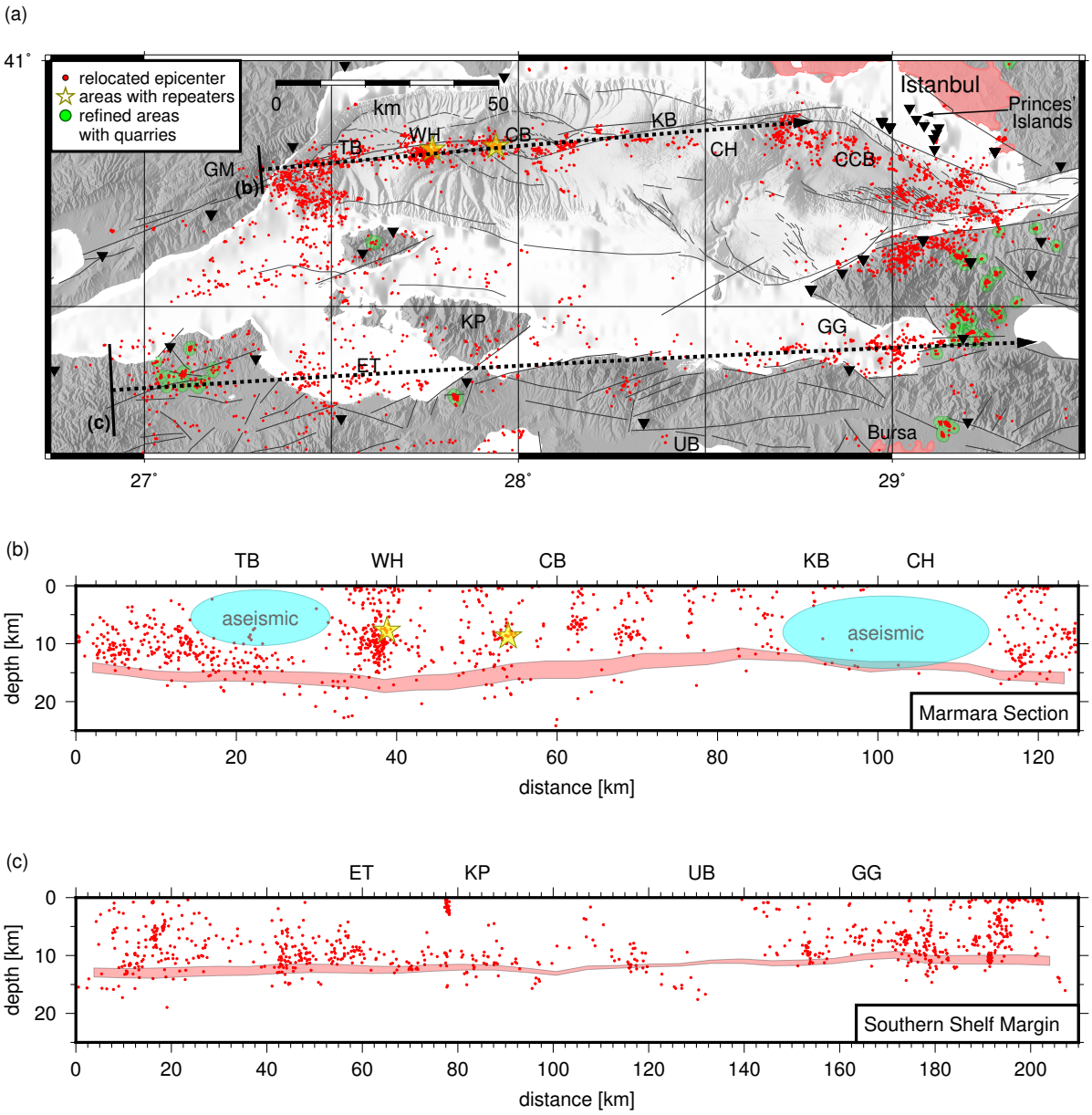

Figure 27: (a) Epicenter map with the surface projections of two east-west trending vertical cross sections containing the seismicity shown in (b) and (c). The extent of the volume included in a cross section is delineated by the dashed black lines where the volume's width is indicated by the orthogonal line at its beginning and the orientation of the cross section by the arrowhead at its end. Areas colored green contain dense epicentral clusters likely corresponding to quarry blasts. b) Depth section along the main northern NAFZ branch below the Sea of Marmara between the Ganos fault and the Istanbul bend. The light-red band delineates the base of the seismogenic layer (see section 4.2 for details). (Caption continues on the next page.)

Figure 27: (Continued caption from previous page.) Cyan colored ellipses indicate aseismic patches of the fault. Abbreviations indicate geographical features as in Fig. 1 and are orthogonally projected onto the central line of the cross section for better orientation. c) Depth section along the main southern NAFZ branch along the southern shore of the Sea of Marmara coinciding with the Southern Shelf Margin.

27a). The Cinarcik Basin (CCB) shows activity down to ∼18 km. Most interestingly, there are two well-defined aseismic patches that show the same characteristics as those recently reported along the Princes' Islands segment [Bohnhoff et al., 2013] and along the combined Izmit-Düzce rupture [Bohnhoff et al., 2016a]. The first aseismic patch extends from the surface down to ∼10 km and is located between the Tekirdak Basin and the Western High (Fig. 27a). The second, located further east below the Central High, even extends down to the base of the seismogenic crust. On the basis of the new absolute hypocenters, both aseismic patches are characterized by sparse seismicity (Fig. 23). Whereas this holds true from the perspective of the original locations for the second aseismic patch, the first is not visible here (Fig. 25). These aseismic patches are of particular interest as they may represent either creeping segments or locked fault asperities and thus potential nucleation points of future ruptures [Bohnhoff et al., 2013, 2016a]. Two doublets of earthquake repeaters were previously found in the vicinity of the Western High and Central Basin (yellow stars in Fig. 27 and 27a) [Bohnhoff et al., 2017b] and they were interpreted to indicate fault creep. However, they appear to be located outside of the here reported aseismic patches. This would imply that there is no indication for creep along the two aseismic patches. They thus can be considered to reflect locked patches of the main NAFZ branch below the Sea of Marmara, thereby representing potential nucleation points of future earthquakes in this region.

The hypocentral depth along the Southern Marmara Shelf is generally slightly shallower than along the Marmara Section and it shows a consistent lower boundary at ∼14 km (Fig. 27b). Lateral variations from west to east are smoother than along the Marmara Section but still do allow to identify active portions throughout the seismogenic layer in the western half (km 0–100 in Fig. 27b) and in the east (km 150–200) and a nearly-aseismic patch around the Uluabad Basin. Since there is less consensus on whether the Southern Marmara Shelf represents a coherent NAFZ fault branch similar to the Marmara Section in the north, we do not further interpret the tectonic role of this aseismic portion.

Eastern Sea of Marmara The seismicity distribution in the eastern Sea of Marmara is shown in Figure 29. There, the NAFZ branches into two main fault strands, the Princes' Islands segment in the north and Yalova-Hersek segment in the south. Both strands bound the pull-apart Cinarcik Basin depocenter which is a half-graben structure with a sedimentary thickness on the order of 3–4 km [Le Pichon et al., 2001, Karabulut et al., 2002, Acarel et al., 2014]. The epicentral distribution in this region allows to identify pronounced seismicity along both fault strands with a lateral extension across

the fault on the order of ∼20 km. Both strands were recently shown to merge towards a single master fault below the base of the seismogenic layer [Bohnhoff et al., 2013]. In order to separate on-fault from off-fault seismicity we plot vertical transects of two different widths along the Princes' Islands segment (Fig. 29a + 29b) and along the Yalova-Hersek segment (Fig. 29c + 29d). For the Princes' Islands segment we identify and confirm the existence of a ∼10 km deep and 40 km long aseismic patch with a slightly deeper extend at its western part (Fig. 29b). This feature is clearly visible also among the new absolute locations but obscured in the merged catalogue by the concentration of seismicity at 7.5 km depth (appendix Fig. 43–51). The Imrali Basin is entirely inactive while the Yalova-Hersek segment hosts an aseismic patch down to 10 km (Fig. 29d). The latter is interpreted to reflect a potential fault asperity similar to that identified along the Princes' Islands segment.

Depth transects perpendicular to the Princes' Islands segment are shown in Fig. 31. They confirm that the actual main fault branch (indicated by thick magenta colored line in Fig. 31) is seismically inactive from the Istanbul bend in the west until 20°10'E longitude in the east (Figs. 31b – 31d). Assuming a southward near vertical dip, some dense seismic activity occurs only near the bottom of the seismogenic layer. West of longitude 29°10' other seismicity along these transects is predominantly observed further south-west and off the presumable fault-plane. The phenomenon of abundant off-fault seismicity has been recently reported for the San Jacinto Fault, California [Ross et al., 2017]. For this seismicity to occur on the main fault, the Princes' Island segment would need to have a dip of nearly 45° from the mapped location of its fault escarpment. Beyond longitude 29°10' (and particularly at the site crossed by profile (f)) the seismicity extends to both sides of the fault. However, the calculated focal mechanisms of earthquakes located west of the Istanbul bend (Fig 34, focal mechanisms 4 and 5) suggest fault planes oriented rather parallel to the Princes' Island segment indicating extensional off-fault structures. Örgülü [2011] describe the Cinarcik Basin as a mature basin in which a through-going fault has developed only recently from "coalescence of short strike-slip segments in en-echelon form". Possibly the formation is not yet fully concluded and the formation process is continued a few km further south of the mapped fault escarpment.

Western Marmara Seismicity along the western Marmara Section is shown in Fig. 33. While the onshore Ganos fault does not show any seismicity, in good accordance with earlier findings of a locked status there (Fig. 33) [Motagh et al., 2007], the offshore portion west of the Tekirdak Basin does show activity throughout the seismogenic layer with an aseismic patch down to 10 km below the Tekirdak Basin itself (Fig. 33a). This is in agreement with findings from Yamamoto et al. [2017]. The depth section across the fault (Fig. 33c) indicates that actually most of the activity is diffuse off-fault activity raising the question whether the actual fault might be aseismic as well and the seismicity reflects activation of minor branches and splay faults. The sparse seismicity along the Southern Marmara Shelf does not allow to clearly discriminate seismically active from inactive patches.

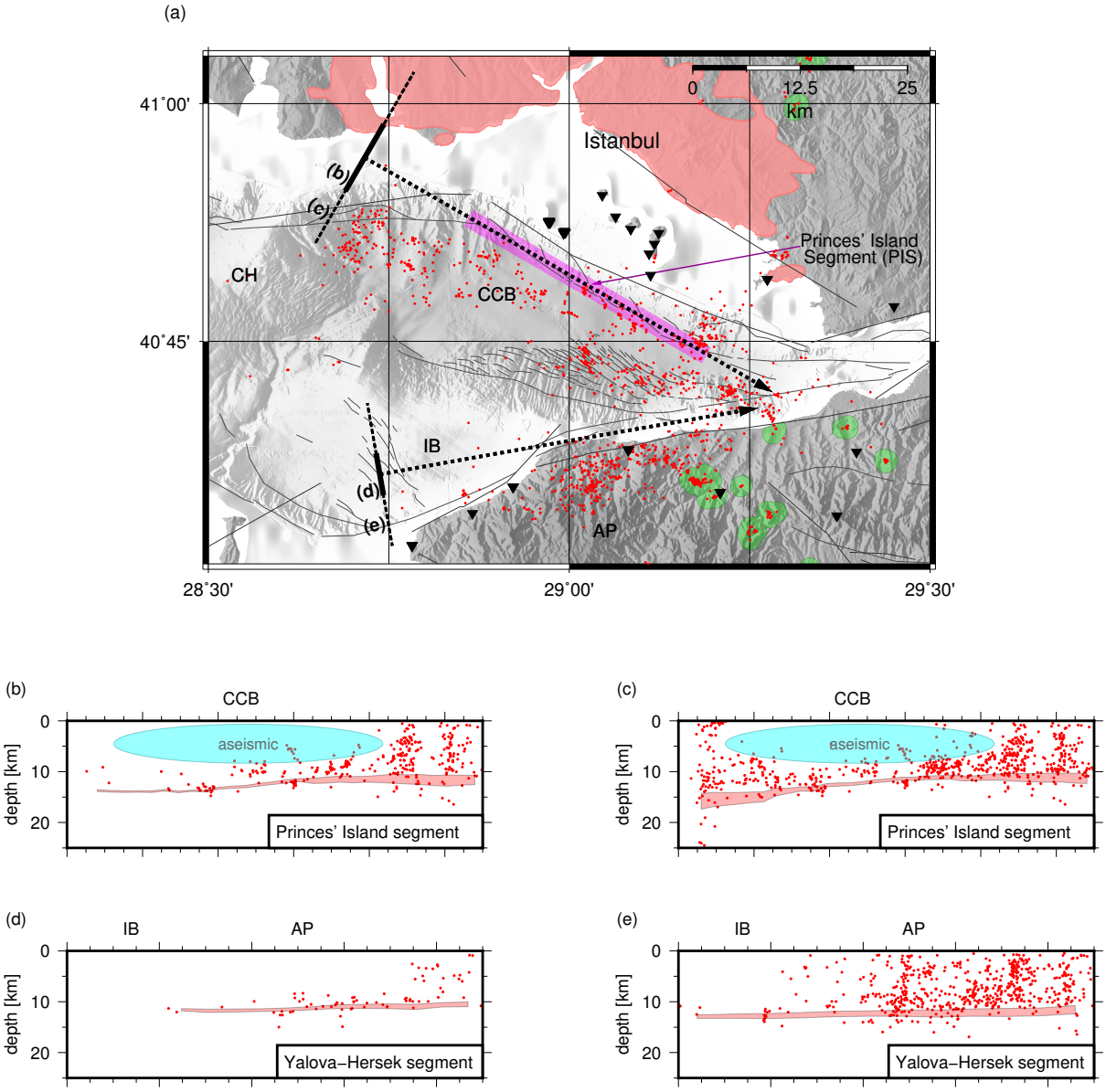

Figure 29: (a) The epicenter map for the eastern Sea of Marmara delineates the surface projections of the vertical cross sections shown in (b)–(e) using the same symbolic scheme as in Fig. 27. The fault escarpment of the Princes' Island Segment (PIS) is marked in magenta. (b) and (c) Cross sections along the Princes' Islands segment between the Istanbul bend and the western termination of the 1999 Izmit rupture with increasing width of the cross-sectional volume. The cyan colored ellipse marks an aseismic patch. (d) and (e) Yalova-Hersek segment at the southern margin of the Imrali Basin, with increasing width of the cross-sectional volume.

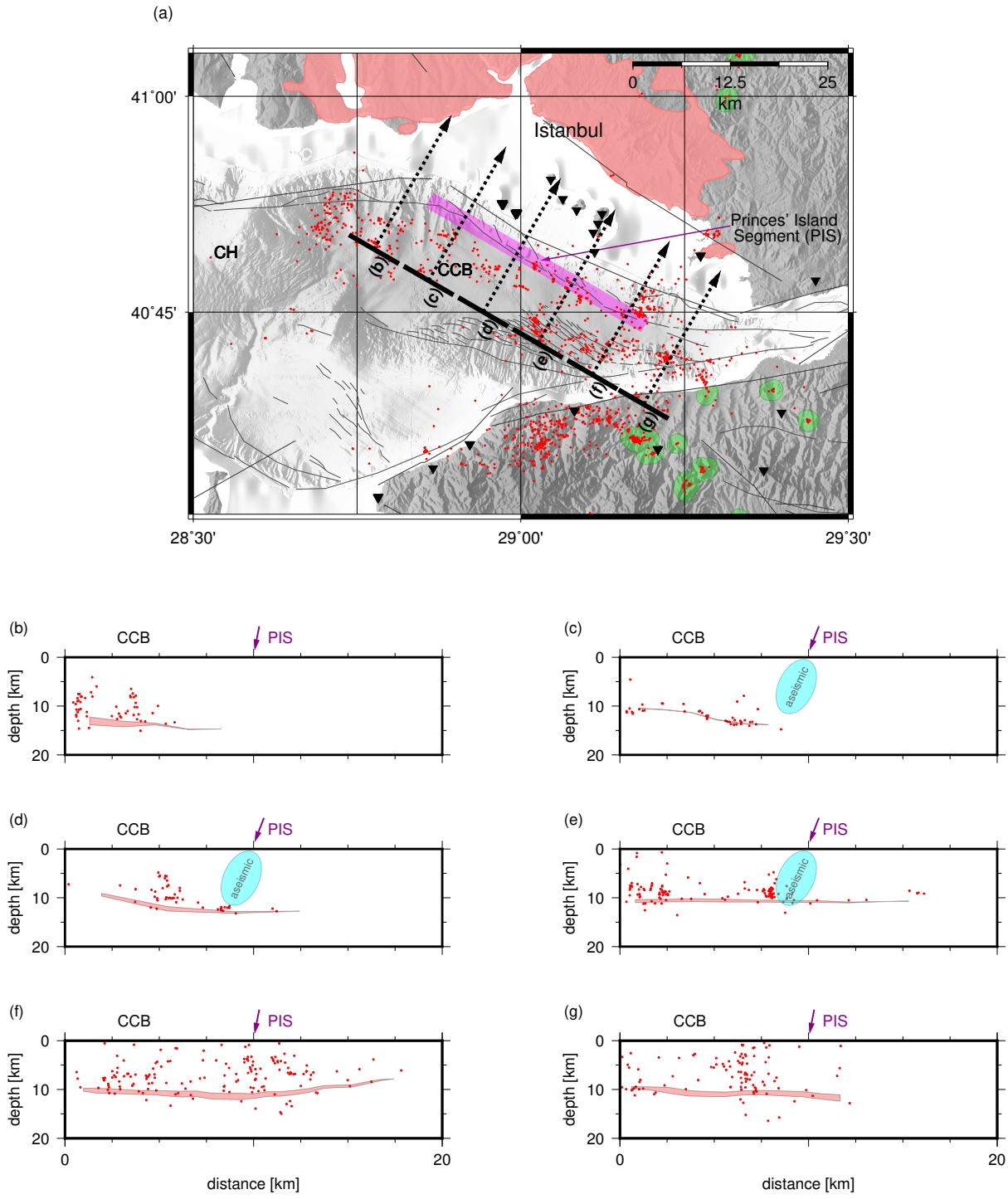

Figure 31: (a) Epicenter map with the surface projections of the vertical cross sections shown in (b)–(g) (cross sections and other symbols as in Fig. 27) where the latter orthogonally strike through the Princes' Islands segment (PIS, also see Fig. 29) and are sorted from West to East. The magenta colored arrow indicates the presumable fault's surface expression and dip (plotted to correspond 80°, note that the angle seems smaller due to the aspect ratio of the figure). The cyan colored ellipse marks an aseismic patch.

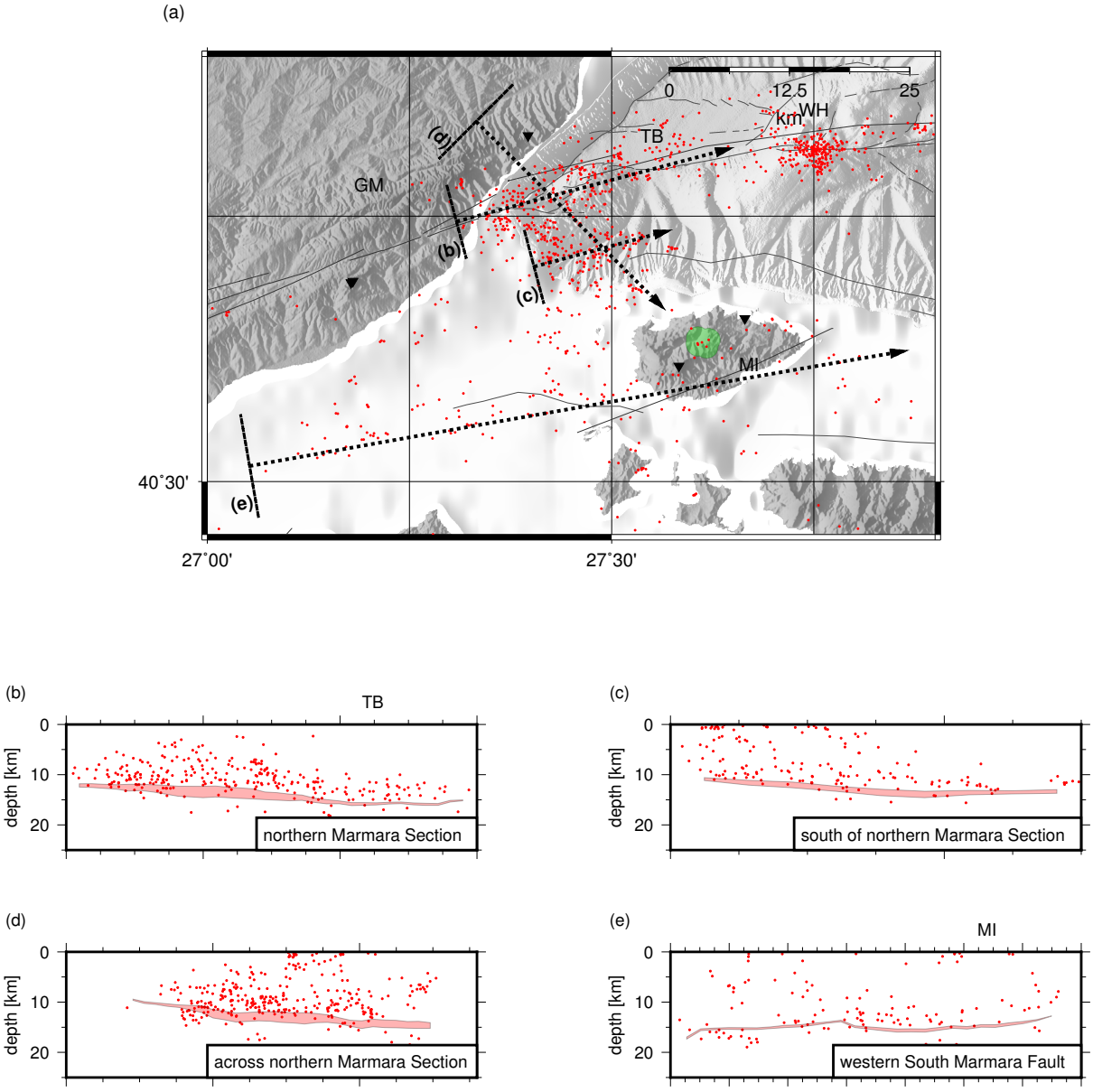

Figure 33: (a) Epicenter map for the western Sea of Marmara at the termination of the Ganos fault with the surface projections of the vertical cross sections shown in (b)–(e) (cross sections and other symbols as in Fig. 27). (b) Western end of the Marmara Section of the northern NAFZ branch coinciding the eastern termination of the 1912 Ganos rupture [Armijo et al., 1999]. (c) Seismicity between the Marmara Section of the northern NAFZ branch and the South Marmara Fault [Le Pichon et al., 2014]. (d) Cross section cutting through the seismicity depicted in (b) and (c). (e) Seismicity at the western end of the South Marmara Fault.

4.3. Identification of locked and creeping fault sections

Locked patches Based on the spatial distribution of seismicity along the Marmara Section as the main NAFZ fault branch extending along the northern Sea of Marmara we can refine the previous understanding of their current nature of deformation (locked versus creeping). Recent seismological and geodetic investigations support the view that the northern branch of the NAFZ, the Marmara Section, currently hosts both locked and creeping fault sections. The onshore Ganos fault immediately to the west of the Sea of Marmara where a M7.4 earthquake occurred in 1912 is currently locked [Motagh et al., 2007, Ergintav et al., 2014, Klein et al., 2017]. This is in good agreement with our results where dominant off-fault seismicity is observed around the Ganos segment (Fig. 33a). Likewise, there are strong indications that the same is true for the Princes' Island Segment offshore Istanbul [Bohnhoff et al., 2013, Ergintav et al., 2014], where the seismic gap down to 10 km depth as reported earlier is confirmed by the here presented hypocenter catalogue.

While the western and eastern portions of the Marmara Section of the NAFZ are comparatively well studied, less information exists for the central part. This is due to the previously less dense distribution of permanent seismic stations there and due to the absence of islands to the south of the fault, preventing from obtaining near-fault GPS measurements. Several aseismic patches previously observed during a tenmonth long OBS-campaign [Yamamoto et al., 2017] can be confirmed to be quiescent over the entire observational period of ten years of this study. Whereas these features are very prominent in our relocated catalogue and can partially also be identified in the catalogue of new absolute locations, the abundant occurrence of seismicity at a fixed depth of 7.5 km in the merged original locations prevents the sight on most of them there. Furthermore, first results from sea-floor based deformation measurements from acoustic extensometers also seem to favor a locked over a creeping status for the Istanbul-Silivri fault segment / Kumburgaz Basin west of Istanbul [Sakic et al., 2016] and below the Western High [Yamamoto et al., 2016].

Creeping patches However, there are also strong indications for creeping sections below parts of the western Marmara Section based on the observation of repeating earthquakes and small b-values around the Central Basin and the Western High [Yamamoto et al., 2016, Schmittbuhl et al., 2016, Bohnhoff et al., 2017b] where creep rates might locally accommodate as much as 25–75% of the plate deformation [Bohnhoff et al., 2017b]. The limitation of repeating earthquakes to the Western High and Central Basin regions establishes a focus on the adjacent areas, i.e. the edges of the central Marmara Section, namely the Tekirdag Basin and the Kumburgaz Basin/Central High region, where larger aseismic patches indicate potentially locked fault segments.

4.4. Focal mechanisms

Based on the here presented 10-year seismicity catalogue, we also determine singleevent focal mechanism solutions for the largest events in order to study the kinematic set-

ting along the principal NAFZ fault branches below the Sea of Marmara. We use the automatically determined P-wave first-motion polarities to calculate a total of 140 focal mechanisms which were calculated for events located with $\geq$ 20 P-picks containing $\geq$ 18 P-wave first motion polarities, $\geq$ 12 S-picks, azimuthal gap $\leq 90^{\circ}$, area of error ellipse $\leq$ 25 km^2, focal depth in the range of [4, 20] km and magnitude Mw $\geq$ 2.7. The inversion was performed with the HASH software [Hardebeck and Shearer, 2002]. The epicenters of all focal mechanisms and 46 beach-balls are shown on a map of the region in Fig. 34 together with selected focal mechanisms previously published [Örgülü, 2011, Öztürk et al., 2015]. The P- and T-axis distribution of all solutions is displayed on a stereographic projection of the lower hemisphere in Fig. 35. Our focal mechanism solutions were divided into four categories of quality according to table 4.

The spread of fault-plane uncertainties is large ($13^{\circ} < \Delta FP < 53^{\circ}$), the average fault plane uncertainty being 37°. The behavior of the uncertainty cannot be unambiguously linked to one cause or parameter. Additionally to the fault-plane uncertainty (in degrees as returned by HASH), we also consider the number of first-motion polarities inverted as a proxy for a focal mechanisms quality (Table 4). However, there is a large spread in the correlation of these two parameters (as well as in the correlation between magnitude and number of first-motion polarities). Apart from falsely picked first-motion polarities, this is likely because the coverage of the focal sphere is not optimal in general and also it varies strongly in between events. However, the inversion scheme is very sensitive to the coverage as well as to the orientation of the true underlying focal plane. For the method employed here smaller uncertainties would first of all require a complete coverage of the focal sphere particularly at its poles. Four of our focal mechanism solutions have been previously determined by Öztürk et al. [2015] too (focal plane # $= 1, 18, 42$ and 46, also see Table 5). The pairs of solutions are congruent. Detailed depiction of our solutions to three previously calculated focal-mechanism solutions, including first-motion polarities and P- and T-axis of all "acceptable solutions" [Hardebeck and Shearer, 2002] are shown in the appendix (Fig. 37, 39 and 40).

The analyzed earthquakes display predominantly near horizontal SW-NE striking T-axis, most P-axis spreading along a band striking NW-SE (Fig. 35). This corresponds to focal mechanisms predominantly ranging in the strike-slip and normal faulting regime with no clear dependence on their magnitude, confirming the earlier findings of a primarily transtensional regime in the larger Marmara region [Armijo et al., 1999, Le Pichon et al., 2001, Bohnhoff et al., 2006]. This observation holds for the NAFZ northern branch from the Western High eastwards to the rupture area of the 1999 Izmit earthquake as well as along the Southern Shelf Margin west of the Gemlik Bay (Fig. 34). The fact that no spatially isolated pure strike-slip or normal faulting segments are observed seems to indicate that there is neither a single through-going strike-slip fault as proposed by Le Pichon et al. [2001] nor a dominantly set of en-echelon normal faulting Armijo et al. [2002]. In contrast, the entire region currently sees both strike-slip and normal faulting along the entire NAFZ section below the Sea of Marmara leaving the question open whether a pending larger earthquake might be one dominantly strike-slip event or a series of smaller normal faulting earthquakes.

Two focal mechanisms were calculated west of the Istanbul bend (numbers 6 and 7 in

Table 4: Table relating color of compressional quadrant of beachballs in Fig. 34 to respective fault plane uncertainty (ΔFP, last column in Table 5) in degrees. N(FP) is the count of fault planes assigned to a certain uncertainty category.

ΔFP	$< 20°$	$< 25°$	$< 35°$	$< 45°$	$\geq 45°$	total	
color							
N(FP)	2	9	28	4	3	46	Fig. 34)
N(FP)	2	8	47	56	27	140	Fig. 35)

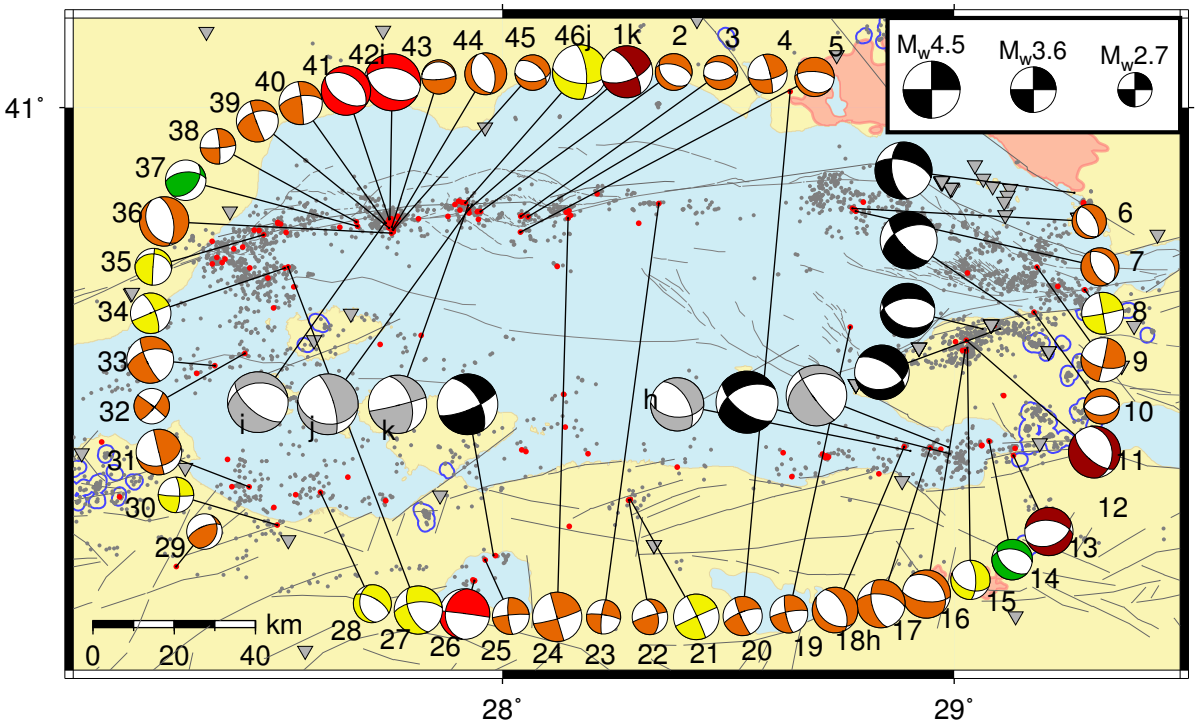

Figure 34: Location of 140 events from Fig. 35 (their P- and T-axis on lower hemisphere) displayed by red circles and focal mechanism solutions for 46 relocated events with moment magnitude $2.7 \leq$ Mw ≤ 4.5 (from the 140 solutions, the 6 largest events and out of the remaining, the 40 best; also see Table 5). The beachball size corresponds to the magnitude. Relocated seismicity (from Fig. 18) is marked by gray dots. The focal mechanisms were chosen according to their solution quality and magnitude (see Section 4.4 for details). The color of the compressive quadrants, green, yellow, orange and red, indicate decreasing quality of a focal plane solution (see Table 4 for the corresponding interval of fault plane uncertainty in degrees). Black and gray focal planes are from Örgülü [2011] and Öztürk et al. [2015], respectively.

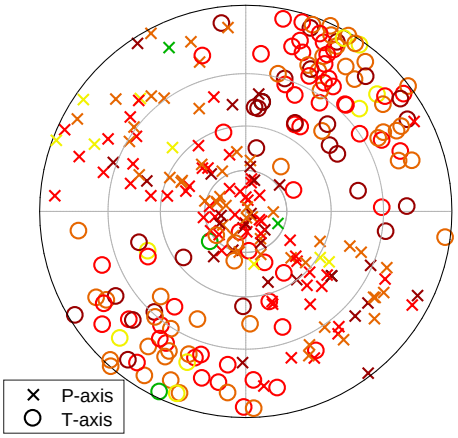

Figure 35: P- and T-axis of 140 fault-plane solutions plotted on a stereographic projection of the lower hemisphere and symbolized by crosses and open circles respectively. The P- and T-axis are color encoded according to the quality of the corresponding fault-plane solution (also see Table 4). The epicenters of the corresponding events are highlighted in Fig. 34.

Fig. 34), being both normal faulting and suggesting that the ruptured faults form a large angle with the main fault trace to the north. This further supports the hypothesis that the seismicity of this region is occurring predominantly off-fault and therefore the main section could be accumulating seismic energy. In contrast, around the Central Basin (focal mechanisms 40, 1, 2, 3) the fault plane striking approximately ∼80° is in good agreement with the main fault trace at this area. This could provide further indication that around the Central Basin the seismicity occurs predominantly on the fault and that a portion of the slip is released aseismically.

Many of the focal mechanisms have a significant reverse component: 25 % measure oblique plunge of the tensional axis ($22.5° < \text{pl(T)} <= 67.5°$), another 4 % near vertical ($\text{pl(T)} <= 22.5°$) reverse components. This result contradicts the large scale picture, that the Sea of Marmara region is dominated by a transtensional stress regime, raising the question of how reliable this is. However, the set of focal mechanisms with thrust components includes such with comparatively small uncertainties (Fig. 38) thus confirming previous observations of local thrust faulting throughout the Sea of Marmara region made by other studies [Pinar et al., 2001, 2003, Bohnhoff et al., 2006, Bulut et al., 2009, Öztürk et al., 2015]. The agglomeration of reverse faulting in the West near the Ganos Bend can be attributed to a transpressional stress-field component which results from the change of strike of the Marmara Section here [Pinar et al., 2003, Janssen et al., 2009, Örgülü, 2011, Öztürk et al., 2015]. In contrast rather sparse reverse faulting in other areas, e.g. the Central Basin as well as around the termination of the 1999 Izmit rupture, is explained with the activation of subsidiary faults, e.g. antithetic Riedel shears developing in vicinity of main E-W striking fault, [Pinar et al., 2003].

5. Conclusions

We present a refined hypocenter catalogue for the Sea of Marmara containing 6812 earthquake locations recorded during a $10\frac{1}{2}$ year period of time in the years 2006–2016. Relative relocation yields a subset of 4407 high precision earthquake locations. We calculate moment magnitudes for 5353 and focal mechanisms for 140 earthquakes. Our results are based on the analysis of recordings from several permanent seismic networks, most importantly of the integrated datasets provided by the two major national seismological services (AFAD and KOERI) running the largest seismological networks in the area. We employed an analysis scheme including automatized timing of P- and S-phases, determination of the P-wave first-motion polarity and an iterative travel-time inversion. Particular caution was exercised during the automatic picking, where results for P- and S-phases were assigned continuous uncertainties and validated with a representative set of manual reference picks.

A previously developed automatized picking scheme was modified and adapted to the here analyzed regional seismicity. Approximately 360,000 P- and S-picks were retrieved and 165,000 crustal first arriving P- and S-phases inverted. With respect to manual reference picks, 68 % of automatic P- and S-picks lie within $\sim$0.1s and $\sim$0.3s, respectively. Despite rigorously discarding seismic recordings without determinable seismic onsets, an iterative travel-time inversion-scheme improves location accuracy by discarding further miss-picked phase onsets. During this procedure, we fall back to phase-pick uncertainties which were calculated with a novel approach employing multiple application of the Akaike-Information-Criterion (AIC) to different windows of a seismic recording that likely contain the targeted seismic onset.

Our absolute (and relatively relocated) earthquake hypocenters make out more than one half (one third) of the $\sim 12,000$ earthquakes reported by the national seismological services and other researchers. We show that the loss affects small earthquakes that were likely recorded by a small fraction of the network only and thus lack sufficient observations needed for precise localization. However, the final relative relocation of hypocenters yields a consistent long-term observation of a decade of regional seismic activity along the Marmara Section of the North Anatolian Fault Zone, during a seismotectonic period that presumably is developing towards a major $M \geq 7$ earthquake posing a significant seismic risk to substantial infrastructure in the Istanbul metropolitan area. Compared to the original merged catalog, our automatized processing chain achieves a substantial improvement particularly of epicentral location accuracy. In areas at close proximity to seismic stations, e.g. the Princes' Island segment, the improvement is distinct also in the vertical. The relative relocation further compacts densely occurring seismicity, revealing linear trends as well as sharpening the contours of its distribution.

The epicentral distribution delineates the Marmara Section of the northern branch of the NAF as the more active compared to the northern most branch of the southern NAF along the Southern Shelf Margin. Three unambiguously identifiable aseismic patches on the Marmara Section raise the question on the cause of this quiescence. Aseismic creep has been deduced from the occurrence of seismic repeaters as well as from large deformation rates measured with acoustic extensometers for some locations in the western half of

the central part of the Marmara Section (Western High, Central Basin). However they are located outside the aseismic patches on which we report here, indicating that they are probably locked fault patches and thus potential nucleation points for the pending Marmara earthquake. Neither repeaters nor large deformation rates are reported for the Princes' Island segment. Seismic activity in the past decade seems to occur off fault and predominantly on the edges of the aseismic patch, supporting previous studies that this fault segment in the immediate vicinity to the Istanbul Metropolitan area is locked. With respect to the E-W orientation of the central Marmara Section, we predominantly observe sub-parallelly striking strike-slip as well as normal faulting mechanisms of parallel and almost orthogonal strike. These mechanisms do not correlate clearly with magnitude, indicating that the region finds itself in a transtensional stress regime. Observation of well resolved reverse faulting mechanisms confirms results of other studies that numerous subsidiary faults exist in the area. This could be attributed to fault stepovers along the Marmara Section and supports the hypothesis of ongoing structure development. Consequently the here presented results show that neither the pure strike-slip nor the normal fault model are supported by the data. Instead a combination of both, with intersecting strike-slip and normal fault segments along the Marmara Section of the NAFZ is suggested by our findings.

Acknowledgements

We thank three anonymous reviewers for the constructive comments. We thank KOERI, Istanbul, and AFAD, Ankara, for providing seismic waveform data from stations throughout the Marmara region. We acknowledge funding from the Helmholtz Association in the frame of the Young Investigators Group SO-053 and Helmholtz Postdoc Programme, and from the German Research Foundation DFG under grant Bo1877/6. We especially thank Filiz Tuba Kadirioğlu, Recai Kartal and Kenan Yanık from AFAD for preparing waveform recordings, Claudius Marx for managing the combined waveform data base, Grzegorz Kwiatek for support with the relocation procedure and Philippe Jousset for the fruitful discussions on the estimation of uncertainties during automatic timing of seismic phases. The Maps and cross sections were plotted with the Generic Mapping Tool (GMT) [Wessel et al., 2013]. The automatic picker was implemented with MATLAB®.

References

References

D. Acarel, F. Bulut, M. Bohnhoff, and R. Kartal. Coseismic velocity change associated with the 2011 Van earthquake (M7.1): Crustal response to a major event. *Geophysical Research Letters*, 41(13):4519–4526, 2014. ISSN 1944-8007.

doi: 10.1002/2014GL060624. URL http://dx.doi.org/10.1002/2014GL060624. 2014GL060624.

H. Akaike. Markovian representation of stochastic processes and its application to the analysis of autoregressive moving average processes. *Annals of the Institute of Statistical Mathematics*, 26(1):363–387, 1974. ISSN 0020-3157. doi: 10.1007/BF02479833. URL http://dx.doi.org/10.1007/BF02479833.

N. N. Ambraseys. Some characteristic features of the Anatolian fault zone. *Tectonophysics*, 9(2–3):143 – 165, 1970. ISSN 0040-1951. doi: http://dx.doi.org/10.1016/0040-1951(70)90014-4. URL http://www.sciencedirect.com/science/article/pii/0040195170900144.

D. J. Andrews. Objective Determination of Source Parameters and Similarity of Earthquakes of Different Size. In *Earthquake Source Mechanics*, pages 259–267. American Geophysical Union, 1986. ISBN 978-1-118-66486-5. URL http://dx.doi.org/10.1029/GM037p0259.

R. Armijo, B. Meyer, A. Hubert, and A. Barka. Westward propagation of the North Anatolian fault into the northern Aegean: Timing and kinematics. *Geology*, 27(3):267, Mar. 1999. doi: 10.1130/0091-7613(1999)027\<0267:WPOTNA\>2.3.CO;2. URL http://geology.gsapubs.org/content/27/3/267.abstract.

R. Armijo, B. Meyer, S. Navarro, G. King, and A. Barka. Asymmetric slip partitioning in the Sea of Marmara pull-apart: A clue to propagation processes of the North Anatolian Fault? *Terra Nova*, 14(2):80–86, 2002. ISSN 1365-3121. doi: 10.1046/j.1365-3121.2002.00397.x. URL http://dx.doi.org/10.1046/j.1365-3121.2002.00397.x.

R. Armijo, N. Pondard, B. Meyer, G. Uçarkus, B. M. de Lépinay, J. Malavieille, S. Dominguez, M.-A. Gustcher, S. Schmidt, C. Beck, N. Çagatay, Z. Çagatay, N.Çakir, C. Imren, K. Eris, B. Natalin, G. Örgülü, S. Özalaybey, L. Tolun, I. Lefèvre, L. Seeber, L. Gasperini, C. Rangin, O. Emre, and K. Sarikavak. Submarine fault scarps in the Sea of Marmara pull-apart (North Anatolian Fault): Implications for seismic hazard in Istanbul. *Geochemistry, Geophysics, Geosystems*, 6(6), 2005. ISSN 1525-2027. doi: 10.1029/2004GC000896. URL http://dx.doi.org/10.1029/2004GC000896.

A. Barka. The north Anatolian fault zone. In *Annales Tectonicae*, volume 6, pages 164–195, 1992.

A. Barka, H. S. Akyüz, E. Altunel, G. Sunal, Z. Çakir, A. Dikbas, B. Yerli, R. Armijo, B. Meyer, J. B. de Chabalier, T. Rockwell, J. R. Dolan, R. Hartleb, T. Dawson, S. Christofferson, A. Tucker, T. Fumal, R. Langridge, H. Stenner, W. Lettis, J. Bachhuber, and W. Page. The Surface Rupture and Slip Distribution of the 17 August 1999 İzmit Earthquake (M 7.4), North Anatolian Fault. *Bulletin of the Seismological Society of America*, 92(1):43, 2002. doi: 10.1785/0120000841. URL +%0020http://dx.doi.org/10.1785/0120000841.

A. Bécel, M. Laigle, B. de Voogd, A. Hirn, T. Taymaz, A. Galvé, H. Shimamura, Y. Murai, J.-C. Lépine, M. Sapin, and S. Özalaybey. Moho, crustal architecture and deep deformation under the North Marmara Trough, from the SEISMARMARA Leg 1 offshore–onshore reflection–refraction survey. *Tectonophysics*, 467(1–4):1 – 21, 2009. ISSN 0040-1951. doi: 10.1016/j.tecto.2008.10.022. URL http://www.sciencedirect.com/science/article/pii/S0040195108005192.

M. Bohnhoff, H.-P. Harjes, and T. Meier. Deformation and stress regimes in the Hellenic subduction zone from focal Mechanisms. *Journal of Seismology*, 9(3):341–366, July 2005. ISSN 1573-157X. doi: 10.1007/s10950-005-8720-5. URL https://doi.org/10.1007/s10950-005-8720-5.

M. Bohnhoff, H. Grosser, and G. Dresen. Strain partitioning and stress rotation at the North Anatolian fault zone from aftershock focal mechanisms of the 1999 Izmit Mw= 7.4 earthquake. *Geophysical Journal International*, 166(1):373–385, 2006. doi: 10.1111/j.1365-246X.2006.03027.x. URL http://dx.doi.org/10.1111/j.1365-246X.2006.03027.x.

M. Bohnhoff, F. Bulut, G. Dresen, P. E. Malin, T. Eken, and M. Aktar. An earthquake gap south of Istanbul. *Nature Communications*, 4, June 2013. URL http://dx.doi.org/10.1038/ncomms2999.

M. Bohnhoff, M. Ickrath, and G. Dresen. Seismicity distribution in conjunction with spatiotemporal variations of coseismic slip and postseismic creep along the combined 1999 Izmit-Düzce rupture. *Tectonophysics*, 686(Supplement C):132 – 145, 2016a. ISSN 0040-1951. doi: https://doi.org/10.1016/j.tecto.2016.07.029. URL http://www.sciencedirect.com/science/article/pii/S0040195116303122.

M. Bohnhoff, P. Martínez-Garzón, F. Bulut, E. Stierle, and Y. Ben-Zion. Maximum earthquake magnitudes along different sections of the North Anatolian fault zone. *Tectonophysics*, 674:147 – 165, 2016b. ISSN 0040-1951. doi: http://dx.doi.org/10.1016/j.tecto.2016.02.028. URL http://www.sciencedirect.com/science/article/pii/S0040195116001256.

M. Bohnhoff, G. Dresen, U. Ceken, F. T. Kadirioglu, R. F. Kartal, T. Kilic, M. Nurlu, K. Yanik, D. Acarel, F. Bulut, H. Ito, W. Johnson, P. E. Malin, and D. Mencin. GONAF – the borehole Geophysical Observatory at the North Anatolian Fault in the eastern Sea of Marmara. *Scientific Drilling*, 22:19–28, 2017a. doi: 10.5194/sd-22-19-2017. URL https://www.sci-dril.net/22/19/2017/.

M. Bohnhoff, C. Wollin, D. Domigall, L. Küperkoch, P. Martínez-Garzón, G. Kwiatek, G. Dresen, and P. E. Malin. Repeating Marmara Sea earthquakes: Indication for fault creep. *Geophysical Journal International*, 210(1):332–339, 2017b. doi: 10.1093/gji/ggx169. URL http://dx.doi.org/10.1093/gji/ggx169.

P. Bormann, D. A. Storchak, and J. Schweitzer. The IASPEI standard nomenclature of seismic phases. In P. Bormann, editor, *New Manual of Seismological Observatory Practice 2 (NMSOP-2)*, pages 1 – 20. Deutsches GeoForschungsZentrum GFZ, Potsdam, 2013. URL 10.2312/GFZ.NMSOP-2_IS_2.1. StandardNomenclatureSeismicPhases.

F. Bulut, M. Bohnhoff, M. Aktar, and G. Dresen. Characterization of aftershock-fault plane orientations of the 1999 İzmit (Turkey) earthquake using high-resolution aftershock locations. *Geophysical Research Letters*, 34(20), 2007. ISSN 1944-8007. doi: 10.1029/2007GL031154. URL http://dx.doi.org/10.1029/2007GL031154.

F. Bulut, M. Bohnhoff, W. L. Ellsworth, M. Aktar, and G. Dresen. Microseismicity at the North Anatolian Fault in the Sea of Marmara offshore Istanbul, NW Turkey. *Journal of Geophysical Research: Solid Earth*, 114(B9), 2009. ISSN 2156-2202. doi: 10.1029/2008JB006244. URL http://dx.doi.org/10.1029/2008JB006244.

F. Bulut, W. L. Ellsworth, M. Bohnhoff, M. Aktar, and G. Dresen. Spatiotemporal Earthquake Clusters along the North Anatolian Fault Zone Offshore İstanbul. *Bulletin of the Seismological Society of America*, 101(4):1759–1768, 2011. doi: 10.1785/0120100215. URL http://www.bssaonline.org/content/101/4/1759.abstract.

F. Bulut, M. Bohnhoff, T. Eken, C. Janssen, T. Kılıç, and G. Dresen. The East Anatolian Fault Zone: Seismotectonic setting and spatiotemporal characteristics of seismicity based on precise earthquake locations. *Journal of Geophysical Research: Solid Earth*, 117(B7), 2012. ISSN 2156-2202. doi: 10.1029/2011JB008966. URL http://dx.doi.org/10.1029/2011JB008966.

E. Cros and L. Geli, L. Caracterisation of microseimicity in the Western Sea of Marmara: Implications in terms of seismic monitoring. Technical report, Ifremer, 2013. URL http://archimer.ifremer.fr/doc/00278/38916/.

A. Şengör, N. Görür, and F. Şarŏglu. Strike-slip faulting and related basin formation in zones of tectonic escape: Turkey as a case study. *Society of Economic Paleontologists and Mineralogists*, 1985.

A. Şengör, O. Tüysüz, C. İmren, M. Sakınç, H. Eyidŏgan, G. Görür, X. Le Pichon, and C. Rangin. The North Anatolian Fault: A new look. *Annual Review of Earth and Planetary Sciences*, 33:37–112, 2005. ISSN 0084-6597. doi: 10.1146/annurev.earth.32.101802.120415.

A. C. Şengör, C. Grall, C. İmren, X. Le Pichon, N. Görür, P. Henry, H. Karabulut, and M. Siyako. The geometry of the North Anatolian transform fault in the Sea of Marmara and its temporal evolution: Implications for the development of intracontinental transform faults. *Canadian Journal of Earth Sciences*, 51(3): 222–242, Feb. 2014. ISSN 0008-4077. doi: 10.1139/cjes-2013-0160. URL http://dx.doi.org/10.1139/cjes-2013-0160.

T. Diehl, E. Kissling, S. Husen, and F. Aldersons. Consistent phase picking for regional tomography models: Application to the greater Alpine region. *Geophysical Journal International*, 176(2):542–554, 2009. doi: 10.1111/j.1365-246x.2008.03985.x. URL http://dx.doi.org/10.1111/j.1365-246x.2008.03985.x.

S. Ergintav, R. E. Reilinger, R. Çakmak, M. Floyd, Z. Cakir, U. Doğan, R. W. King, S. McClusky, and H. Özener. Istanbul's earthquake hot spots: Geodetic constraints on strain accumulation along faults in the Marmara seismic gap. *Geophysical Research Letters*, 41(16):5783–5788, 2014. ISSN 1944-8007. doi: 10.1002/2014GL060985. URL http://dx.doi.org/10.1002/2014GL060985. 2014GL060985.

M. Ester, H.-P. Kriegel, J. Sander, and X. Xu. A density-based algorithm for discovering clusters in large spatial databases with noise. pages 226–231. AAAI Press, 1996.

F. Flerit, R. Armijo, G. King, and B. Meyer. The mechanical interaction between the propagating North Anatolian Fault and the back-arc extension in the Aegean. *Earth and Planetary Science Letters*, 224(3):347 – 362, 2004. ISSN 0012-821X. doi: https://doi.org/10.1016/j.epsl.2004.05.028. URL http://www.sciencedirect.com/science/article/pii/S0012821X04003486.

L. Geiger. Probability method for the determination of earthquake epicenters from the arrival time only. *Bull. St. Louis Univ*, 8(1):56–71, 1912.

F. Grigoli, S. Cesca, O. Amoroso, A. Emolo, A. Zollo, and T. Dahm. Automated seismic event location by waveform coherence analysis. *Geophysical Journal International*, 196 (3):1742, 2014. doi: 10.1093/gji/ggt477. URL http://dx.doi.org/10.1093/gji/ggt477.

T. C. Hanks and H. Kanamori. A moment magnitude scale. *Journal of Geophysical Research: Solid Earth*, 84(B5):2348–2350, 1979. ISSN 2156-2202. doi: 10.1029/JB084iB05p02348. URL http://dx.doi.org/10.1029/JB084iB05p02348.

J. L. Hardebeck and P. M. Shearer. A New Method for Determining First-Motion Focal Mechanisms. *BULLETIN OF THE SEISMOLOGICAL SOCIETY OF AMERICA*, 92(6):2264–2276, Aug. 2002. doi: 10.1785/0120010200. URL http://dx.doi.org/10.1785/0120010200.

T. Hergert and O. Heidbach. Slip-rate variability and distributed deformation in the Marmara Sea fault system. *Nature Geosci*, 3(2):132–135, Feb. 2010. ISSN 1752-0894. doi: 10.1038/ngeo739. URL http://dx.doi.org/10.1038/ngeo739.

C. Janssen, M. Bohnhoff, Y. Vapnik, E. Görgün, F. Bulut, B. Plessen, D. Pohl, M. Aktar, A. I. Okay, and G. Dresen. Tectonic evolution of the Ganos segment of the North Anatolian Fault (NW Turkey). *Journal of Structural Geology*, 31(1):11 – 28, 2009. ISSN 0191-8141. doi: http://dx.doi.org/10.1016/j.jsg.2008.09.010. URL http://www.sciencedirect.com/science/article/pii/S0191814108001636.

P. Jousset, A. Budi-Santoso, A. D. Jolly, M. Boichu, Surono, S. Dwiyono, S. Sumarti, S. Hidayati, and P. Thierry. Signs of magma ascent in {LP} and {VLP} seismic events and link to degassing: An example from the 2010 explosive eruption at Merapi volcano, Indonesia. *Journal of Volcanology and Geothermal Research*, 261:171 – 192, 2013. ISSN 0377-0273. doi: http://dx.doi.org/10.1016/j.jvolgeores.2013.03.014. URL http://www.sciencedirect.com/science/article/pii/S0377027313000905. Merapi eruption.

H. Karabulut, M.-P. Bouin, M. Bouchon, M. Dietrich, C. Cornou, and M. Aktar. The Seismicity in the Eastern Marmara Sea after the 17 August 1999 İzmit Earthquake. *Bulletin of the Seismological Society of America*, 92(1):387–393, 2002. ISSN 0037-1106. doi: 10.1785/0120000820. URL http://bssa.geoscienceworld.org/content/92/1/387.

H. Karabulut, J. Schmittbuhl, S. Özalaybey, O. Lengliné, A. Kömeç-Mutlu, V. Durand, M. Bouchon, G. Daniel, and M. P. Bouin. Evolution of the seismicity in the eastern Marmara Sea a decade before and after the 17 August 1999 Izmit earthquake. *Tectonophysics*, 510(1–2):17 – 27, 2011. ISSN 0040-1951. doi: http://dx.doi.org/10.1016/j.tecto.2011.07.009. URL http://www.sciencedirect.com/science/article/pii/S0040195111002903.

I. Ketin. Über die tektonisch-mechanischen Folgerungen aus den großen anatolischen Erdbeben des letzten Dezenniums. *Geologische Rundschau*, 36(1):77–83, Dec. 1948. ISSN 1432-1149. doi: 10.1007/BF01791916. URL https://doi.org/10.1007/BF01791916.

J. Kinscher, F. Krger, H. Woith, B. Lhr, E. Hintersberger, T. Irmak, and S. Baris. Seismotectonics of the armutlu peninsula (marmara sea, nw turkey) from geological field observation and regional moment tensor inversion. *Tectonophysics*, 608:980 – 995, 2013. ISSN 0040-1951. doi: http://dx.doi.org/10.1016/j.tecto.2013.07.016. URL http://www.sciencedirect.com/science/article/pii/S0040195113004575.

E. Klein, Z. Duputel, F. Masson, H. Yavasoglu, and P. Agram. Aseismic slip and seismogenic coupling in the Marmara Sea: What can we learn from onland geodesy? *Geophysical Research Letters*, 44(7):3100–3108, 2017. ISSN 1944-8007. doi: 10.1002/2017GL072777. URL http://dx.doi.org/10.1002/2017GL072777. 2017GL072777.

L. Küperkoch. *Automated Recognition, Phase Arrival Time Estimation, and Location of Local and Regional Earthquakes.* dissertation, Ruhr-Universität Bochum, 2011. URL http://www-brs.ub.ruhr-uni-bochum.de/netahtml/HSS/Diss/KueperkochLudger/diss.pdf.

L. Küperkoch, T. Meier, J. Lee, W. Friederich, and E. Working Group. Automated determination of P-phase arrival times at regional and local distances using higher order statistics. *Geophysical Journal International*, 181(2):1159–1170, 2010. ISSN

1365-246X. doi: 10.1111/j.1365-246X.2010.04570.x. URL http://dx.doi.org/10.1111/j.1365-246X.2010.04570.x.

L. Küperkoch, T. Meier, A. Brüstle, J. Lee, W. Friederich, and E. W. Group. Automated determination of S-phase arrival times using autoregressive prediction: Application to local and regional distances. *Geophysical Journal International*, 188(2):687–702, Feb. 2012. doi: 10.1111/j.1365-246x.2011.05292.x. URL http://dx.doi.org/10.1111/j.1365-246x.2011.05292.x.

X. Le Pichon, A. Şengör, and T. Taymaz. The Marmara fault and the future Istanbul earthquake. In M. Karaca and D. N. Ural, editors, *ITU-IAHS International Conference on the Kocaeli Earthquake 17 August 1999*, pages 41–54. Istanbul Technical University, Turkey, 1999. URL http://ci.nii.ac.jp/naid/10006711898/en/.

X. Le Pichon, A. Şengör, E. Demirbağ, C. Rangin, C. Imren, R. Armijo, N. Görür, N. Çağatay, B. M. De Lepinay, B. Meyer, R. Saatçılare, and B. Tok. The active Main Marmara Fault. *Earth and Planetary Science Letters*, 192(4):595 – 616, 2001. ISSN 0012-821X. doi: http://dx.doi.org/10.1016/S0012-821X(01)00449-6. URL http://www.sciencedirect.com/science/article/pii/S0012821X01004496.

X. Le Pichon, N. Chamot-Rooke, C. Rangin, and A. M. C. Sengör. The North Anatolian fault in the Sea of Marmara. *Journal of Geophysical Research: Solid Earth*, 108(B4), 2003. ISSN 2156-2202. doi: 10.1029/2002JB001862. URL http://dx.doi.org/10.1029/2002JB001862. 2179.

X. Le Pichon, C. İmren, C. Rangin, A. Şengör, and M. Siyako. The South Marmara Fault. *International Journal of Earth Sciences*, 103(1):219–231, 2014. ISSN 1437-3254. doi: 10.1007/s00531-013-0950-0. URL http://dx.doi.org/10.1007/s00531-013-0950-0.

X. Le Pichon, A. Şengör, J. Kende, C. İmren, P. Henry, C. Grall, and H. Karabulut. Propagation of a strike slip plate boundary within an extensional environment: The westward propagation of the North Anatolian Fault. *Canadian Journal of Earth Sciences*, 0(ja):null, 2015. doi: 10.1139/cjes-2015-0129. URL http://dx.doi.org/10.1139/cjes-2015-0129.

N. Maeda. A Method for Reading and Checking Phase Time in Auto-Processing System of Seismic Wave Data. *Zisin (Journal of the Seismological Society of Japan. 2nd ser.)*, 38(3):365–379, 1985. doi: 10.4294/zisin1948.38.3_365.

M. Motagh, J. Hoffmann, B. Kampes, M. Baes, and J. Zschau. Strain accumulation across the Gazikoy–Saros segment of the North Anatolian Fault inferred from Persistent Scatterer Interferometry and GPS measurements. *Earth and Planetary Science Letters*, 255(3):432 – 444, 2007. ISSN 0012-821X. doi: http://dx.doi.org/10.1016/j.epsl.2007.01.003. URL http://www.sciencedirect.com/science/article/pii/S0012821X07000040.

M. Murru, A. Akinci, G. Falcone, S. Pucci, R. Console, and T. Parsons. M≥7 earthquake rupture forecast and time-dependent probability for the sea of Marmara region, Turkey. *Journal of Geophysical Research: Solid Earth*, 121(4):2679–2707, 2016. ISSN 2169-9356. doi: 10.1002/2015JB012595. URL http://dx.doi.org/10.1002/2015JB012595. 2015JB012595.

B. Najdahmadi, M. Bohnhoff, and Y. Ben-Zion. Bimaterial interfaces at the Karadere segment of the North Anatolian Fault, northwestern Turkey. *Journal of Geophysical Research: Solid Earth*, 121(2):931–950, 2016. ISSN 2169-9356. doi: 10.1002/2015JB012601. URL http://dx.doi.org/10.1002/2015JB012601. 2015JB012601.

G. Örgülü. Seismicity and source parameters for small-scale earthquakes along the splays of the North Anatolian Fault (NAF) in the Marmara Sea. *Geophysical Journal International*, 184(1):385–404, 2011. doi: 10.1111/j.1365-246X.2010.04844.x. URL http://gji.oxfordjournals.org/content/184/1/385.abstract.

Y. K. Öztürk, N. M. Özal, and A. D. Özbakir. States of local stresses in the Sea of Marmara through the analysis of large numbers of small earthquakes. *Tectonophysics*, 665:37 – 57, 2015. ISSN 0040-1951. doi: http://dx.doi.org/10.1016/j.tecto.2015.09.027. URL http://www.sciencedirect.com/science/article/pii/S0040195115005284.

R. Page. Aftershocks and microaftershocks of the great alaska earthquake of 1964. *Bull. Seismol. Soc. Am.*, 58(3):1131–1168, 1968. cited By 168.

T. Parsons. Recalculated probability of M7 earthquakes beneath the Sea of Marmara, Turkey. *Journal of Geophysical Research: Solid Earth*, 109(B5), 2004. ISSN 2156-2202. doi: 10.1029/2003JB002667. URL http://dx.doi.org/10.1029/2003JB002667. B05304.

A. Pinar, Y. Honkura, and K. Kuge. Seismic activity triggered by the 1999 Izmit earthquake and its implications for the assessment of future seismic risk. *Geophysical Journal International*, 146(1):F1–F7, 2001. ISSN 1365-246X. doi: 10.1046/j.0956-540x.2001.01476.x. URL http://dx.doi.org/10.1046/j.0956-540x.2001.01476.x.

A. Pinar, K. Kuge, and Y. Honkura. Moment tensor inversion of recent small to moderate sized earthquakes: Implications for seismic hazard and active tectonics beneath the Sea of Marmara. *Geophysical Journal International*, 153(1):133–145, 2003. doi: 10.1046/j.1365-246X.2003.01897.x. URL +%0020http://dx.doi.org/10.1046/j.1365-246X.2003.01897.x.

B. Prevedel, F. Bulut, M. Bohnhoff, C. Raub, R. F. Kartal, F. Alver, and P. E. Malin. Downhole geophysical observatories: Best installation practices and a case history from Turkey. *International Journal of Earth Sciences*, 104(6):1537–1547, Sept. 2015.

ISSN 1437-3262. doi: 10.1007/s00531-015-1147-5. URL https://doi.org/10.1007/s00531-015-1147-5.

C. Raub, M. Bohnhoff, B. Petrovic, S. Parolai, P. Malin, K. Yanik, R. F. Kartal, and T. Kiliç. Seismic-Wave Propagation in Shallow Layers at the GONAF-Tuzla Site, Istanbul, Turkey. *Bulletin of the Seismological Society of America*, 2016. ISSN 0037-1106. doi: 10.1785/0120150216. URL http://bssa.geoscienceworld.org/content/early/2016/05/20/0120150216.

C. Raub, P. Martínez-Garzón, G. Kwiatek, M. Bohnhoff, and G. Dresen. Variations of seismic b-value at different stages of the seismic cycle along the North Anatolian Fault Zone in northwestern Turkey. *Tectonophysics*, 712:232 – 248, 2017. ISSN 0040-1951. doi: http://dx.doi.org/10.1016/j.tecto.2017.05.028. URL http://www.sciencedirect.com/science/article/pii/S0040195117302251.

R. Reilinger, S. McClusky, P. Vernant, S. Lawrence, S. Ergintav, R. Cakmak, H. Ozener, F. Kadirov, I. Guliev, R. Stepanyan, M. Nadariya, G. Hahubia, S. Mahmoud, K. Sakr, A. ArRajehi, D. Paradissis, A. Al-Aydrus, M. Prilepin, T. Guseva, E. Evren, A. Dmitrotsa, S. V. Filikov, F. Gomez, R. Al-Ghazzi, and G. Karam. GPS constraints on continental deformation in the Africa-Arabia-Eurasia continental collision zone and implications for the dynamics of plate interactions. *Journal of Geophysical Research: Solid Earth*, 111(B5), 2006. ISSN 2156-2202. doi: 10.1029/2005JB004051. URL http://dx.doi.org/10.1029/2005JB004051. B05411.

Z. E. Ross and Y. Ben-Zion. Automatic picking of direct P, S seismic phases and fault zone head waves. *Geophysical Journal International*, 199(1):368–381, 2014. doi: 10.1093/gji/ggu267. URL +%0020http://dx.doi.org/10.1093/gji/ggu267.

Z. E. Ross, E. Hauksson, and Y. Ben-Zion. Abundant off-fault seismicity and orthogonal structures in the san jacinto fault zone. *Science Advances*, 3(3), 2017. doi: 10.1126/sciadv.1601946. URL http://advances.sciencemag.org/content/3/3/e1601946.

P. Sakic, H. Piété, V. Ballu, J.-Y. Royer, H. Kopp, D. Lange, F. Petersen, M. S. Özeren, S. Ergintav, L. Geli, P. Henry, and A. Deschamps. No significant steady state surface creep along the North Anatolian Fault offshore Istanbul: Results of 6 months of seafloor acoustic ranging. *Geophysical Research Letters*, 43(13):6817–6825, 2016. ISSN 1944-8007. doi: 10.1002/2016GL069600. URL http://dx.doi.org/10.1002/2016GL069600. 2016GL069600.

T. Sato, J. Kasahara, T. Taymaz, M. Ito, A. Kamimura, T. Hayakawa, and O. Tan. A study of microearthquake seismicity and focal mechanisms within the Sea of Marmara (NW Turkey) using ocean bottom seismometers (OBSs). *Tectonophysics*, 391(1):303 – 314, 2004. ISSN 0040-1951. doi: https://doi.org/10.1016/j.tecto.2004.07.018. URL http://www.sciencedirect.com/science/article/pii/S0040195104002379. Active Faulting and Crustal Deformation in the Eastern Mediterranean Region.

J. Schmittbuhl, H. Karabulut, O. Lengliné, and M. Bouchon. Seismicity distribution and locking depth along the Main Marmara Fault, Turkey. *Geochemistry, Geophysics, Geosystems*, 17(3):954–965, 2015. ISSN 1525-2027. doi: 10.1002/2015GC006120. URL http://dx.doi.org/10.1002/2015GC006120.

J. Schmittbuhl, H. Karabulut, O. Lengliné, and M. Bouchon. Long-lasting seismic repeaters in the Central Basin of the Main Marmara Fault. *Geophysical Research Letters*, 43(18):9527–9534, 2016. ISSN 1944-8007. doi: 10.1002/2016GL070505. URL http://dx.doi.org/10.1002/2016GL070505. 2016GL070505.

J. Schweitzer. HYPOSAT — An Enhanced Routine to Locate Seismic Events. In F. Ringdal and B. L. N. Kennett, editors, *Monitoring the Comprehensive Nuclear-Test-Ban Treaty: Sourse Location*, pages 277–289. Birkhäuser Basel, Basel, 2001. ISBN 978-3-0348-8250-7. doi: 10.1007/978-3-0348-8250-7_17. URL https://doi.org/10.1007/978-3-0348-8250-7_17.

P. M. Shearer. *Introduction to Seismology*. Cambridge University Press, Cambridge, 1999. ISBN 0-521-66953-7. URL http://www.worldcat.org/isbn/0521669537.

C. Sippl, B. Schurr, X. Yuan, J. Mechie, F. M. Schneider, M. Gadoev, S. Orunbaev, I. Oimahmadov, C. Haberland, U. Abdybachaev, V. Minaev, S. Negmatullaev, and N. Radjabov. Geometry of the Pamir-Hindu Kush intermediate-depth earthquake zone from local seismic data. *Journal of Geophysical Research: Solid Earth*, 118(4): 1438–1457, 2013. ISSN 2169-9356. doi: 10.1002/jgrb.50128. URL http://dx.doi.org/10.1002/jgrb.50128.

J. A. Snoke. Stable determination of (Brune) stress drops. *Bulletin of the Seismological Society of America*, 77(2):530–538, 1987. URL http://www.bssaonline.org/content/77/2/530.abstract.

D. A. Storchak, J. Schweitzer, and P. Bormann. The IASPEI standard seismic phase list. *Seismological Research Letters*, 74(6):761–772, 2003. ISSN 0895-0695. doi: 10.1785/gssrl.74.6.761. URL http://dx.doi.org/10.1785/gssrl.74.6.761.

J. B. Tary, L. Géli, P. Henry, B. Natalin, L. Gasperini, M. Çomoğlu, N. Çağatay, and T. Bardainne. Sea-Bottom Observations from the Western Escarpment of the Sea of Marmara. *Bulletin of the Seismological Society of America*, 101(2):775, 2011. doi: 10.1785/0120100014. URL +%0020http://dx.doi.org/10.1785/0120100014.

R. Tibi, G. Bock, Y. Xia, M. Baumbach, H. Grosser, C. Milkereit, S. Karakisa, S. Zünbül, R. Kind, and J. Zschau. Rupture processes of the 1999 August 17 Izmit and November 12 Düzce (Turkey) earthquakes. *Geophysical Journal International*, 144(2):F1–F7, 2001. ISSN 1365-246X. doi: 10.1046/j.1365-246x.2001.00360.x. URL http://dx.doi.org/10.1046/j.1365-246x.2001.00360.x.

J. E. Vidale. Complex polarization analysis of particle motion. *Bulletin of the Seismological Society of America*, 76(5):1393–1405, Oct. 1986. ISSN 0037-1106. URL http://dx.doi.org/.

F. Waldhauser and W. L. Ellsworth. A Double-Difference Earthquake Location Algorithm: Method and Application to the Northern Hayward Fault, California. *Bulletin of the Seismological Society of America*, 90(6):1353–1368, 2000. ISSN 0037-1106. doi: 10.1785/0120000006. URL http://bssa.geoscienceworld.org/content/90/6/1353.

P. Wessel, W. H. F. Smith, R. Scharroo, J. Luis, and F. Wobbe. Generic mapping tools: Improved version released. *Eos, Transactions American Geophysical Union*, 94(45):409–410, 2013. ISSN 2324-9250. doi: 10.1002/2013EO450001. URL http://dx.doi.org/10.1002/2013EO450001.

S. Wiemer and M. Wyss. Minimum magnitude of completeness in earthquake catalogs: Examples from alaska, the western united states, and japan. *Bulletin of the Seismological Society of America*, 90(4):859, 2000. doi: 10.1785/0119990114. URL http://dx.doi.org/10.1785/0119990114.

R. Yamamoto, M. Kido, Y. Ohta, N. Takahashi, Y. Yamamoto, D. Kalafat, A. Pinar, H. Ozener, M. S. Ozeren, and K. Yoshiyuki. Estimating slip deficit of the North Anatolian Fault beneath the Sea of Marmara, Turkey, using on- and off-shore geodetic data. *AGU Fall Meeting Abstracts*, Dec. 2016.

Y. Yamamoto, N. Takahashi, A. Pinar, D. Kalafat, S. Citak, M. Comoglu, R. Polat, and Y. Kaneda. Geometry and segmentation of the North Anatolian Fault beneath the Marmara Sea, Turkey, deduced from long-term ocean bottom seismographic observations. *Journal of Geophysical Research: Solid Earth*, 2017. ISSN 2169-9356. doi: 10.1002/2016JB013608. URL http://dx.doi.org/10.1002/2016JB013608. 2016JB013608.

H. Zhang, C. Thurber, and C. Rowe. Automatic P-Wave Arrival Detection and Picking with Multiscale Wavelet Analysis for Single-Component Recordings. *Bulletin of the Seismological Society of America*, 93(5):1904–1912, 2003. doi: 10.1785/0120020241. URL http://www.bssaonline.org/content/93/5/1904.abstract.

A. Kurtosis and Akaike Information Criterion

Kurtosis Küperkoch et al. [2010] showed that in contrast to other characteristic functions like for instance the short-term average over long-term average (STA/LTA), the kurtosis calculated on a window causally running over the filtered waveform is not only sensitive to amplitude but also to frequency and phase changes, and thus can be used as a characteristic function (CF) to amplify also very subtle onsets of seismic signals. In order to pick the first incoming P-wave we calculated the causally running kurtosis of a vertical recording possibly containing the entire wave-train of the event. The kurtosis K for a statistical process sampled by $x = [x_1, ..., x_N]$ equals the quotient of the fourth and the squared second statistical moment, $\mu^{(4)}$ and $\mu^{(2)^2}$ respectively,

$$K = \frac{\mu^{(4)}}{\mu^{(2)^2}} = \frac{\sum_{j=1}^{N} \left(x_j - \bar{x}\right)^4}{\left(\sum_{j=1}^{N} \left(x_j - \bar{x}\right)^2\right)^2} \tag{1}$$

where $\bar{x}$ represents the mean value of the suit of samples. As such the kurtosis describes the tails of a statistical process, i.e. for instance compared to a statistical process whose values obey a Gaussian probability distribution, another statistical process will have a higher kurtosis if it produces more extreme occurrences. The maximum of the running kurtosis time series thus serves as a refined trigger crudely estimating the P-phase arrival. This first step is illustrated in the uppermost row (Z-component) in Fig. 4, showing a 30 s long three component recording.

AIC In order to determine precisely the onset of the seismic phase, the wavelet was then cut 10 s prior and after the kurtosis' maximum. As depicted in Fig. 6 this time window of the wavelet was then used to calculate a suit of AIC-functions after [Maeda, 1985]. Maeda's representation of the AIC is a time series too, which essentially measures the relative misfit of statistical models assuming that the waveform is composed of two consecutive portions, the first being white noise which is then succeeded by an emerging signal. This time series ideally yields a global minimum at the moment of the signal onset. The k^{th} sample of the AIC applied to a real discrete time series $x = [x_1, ..., x_N]$ is defined as

$$aic_k(x) = k \log(var_{1,k}(x)) + (N - k) \log(var_{k+1,N}(x)) \tag{2}$$

where $var_{n,k}(x) = var([x_n, ..., x_k]) = \mu^{(2)}([x_n, ..., x_k])$ is the variance (or the second statistical moment) of x restricted to the interval from n^{th} to k^{th} sample. It has been frequently used to determine the onset of seismic signals in other automatized picking algorithms [Zhang et al., 2003] or as visual picking assistance to a human operator [Jousset et al., 2013].

Table 5: Table of earthquakes for which focal plane solutions are presented in Fig. 34 where they can be identified by the index given the first column (#). The faultplane uncertainty and the number of first-motion polarities used to calculate the focal plane solution are given in the last two columns, ΔFP and N(FM), respectively. Focal plane solutions that can also be found in Öztürk et al. [2015] are highlighted in dark gray.

#	eventID	origin time	M_W	longitude	latitude	depth	strike	dip	rake	ΔFP	N(FM)
1	2013331000004	2013.11.27 04:13:37	4.1	27.9250	40.8290	9.00	70	62	-155	53	39
2	2016084000000	2016.03.24 08:04:59	2.9	27.9517	40.8255	8.34	285	56	-107	31	21
3	2010064000003	2010.03.05 17:31:55	2.7	28.0405	40.8173	7.47	82	54	-108	28	22
4	2008204000001	2008.07.22 10:04:01	3.1	28.0563	40.8168	9.00	80	67	-170	30	19
5	2016030000000	2016.01.30 09:03:14	3.1	28.0397	40.7910	11.02	274	67	-103	30	27
6	2015320000004	2015.11.16 16:36:25	2.7	28.7748	40.8308	8.90	330	60	-90	31	27
7	2015320000006	2015.11.16 17:04:13	3.0	28.7820	40.8260	9.57	316	33	-105	26	26
8	2015225000001	2015.08.13 01:01:29	3.3	29.2888	40.6938	11.97	80	87	-179	20	36
9	2008296000001	2008.10.22 01:00:36	3.5	29.1827	40.7320	9.40	104	62	-177	31	23
10	2009193000000	2009.07.12 06:59:12	2.8	29.1765	40.6563	11.19	88	47	-89	31	20
11	2008072000002	2008.03.12 18:53:32	4.1	29.0267	40.6087	13.74	132	64	-110	48	23
12	2011020000000	2011.01.20 02:09:37	3.8	29.8102	40.6945	14.70	292	68	178	42	24
13	2013229000001	2013.08.17 18:16:31	3.8	29.1310	40.4140	9.00	67	42	-113	56	27
14	2015339000005	2015.12.05 20:53:52	3.2	29.0773	40.4383	12.21	277	46	-116	19	42
15	2009011000001	2009.01.11 06:07:19	3.1	29.0290	40.5960	1.31	110	47	-149	21	25
16	2008279000000	2008.10.05 06:04:05	3.8	29.0242	40.5920	12.72	96	64	-111	30	22
17	2010162000001	2010.06.11 10:56:45	3.8	28.9468	40.4268	9.74	278	57	-143	30	23
18	2011228000001	2011.08.16 17:30:07	3.6	28.8890	40.4288	7.62	126	37	-113	27	26
19	2010013000001	2010.01.13 03:54:52	3.0	28.7700	40.6310	11.37	260	80	-167	29	31
20	2012293000000	2012.10.19 08:17:25	3.1	28.6370	41.0270	11.57	249	73	-172	31	26
21	2009213000003	2009.08.01 16:42:39	3.6	28.2832	40.3395	12.80	246	88	177	23	30
22	2009214000001	2009.08.02 01:21:08	2.8	28.2797	40.3387	12.19	254	84	142	31	35
23	2008203000000	2008.07.21 00:32:24	2.7	28.3460	40.8390	11.69	278	80	-170	28	23
24	2010276000003	2010.10.03 17:49:04	3.9	28.1455	40.8143	10.78	74	84	179	28	36
25	2011214000001	2011.08.02 04:42:30	2.9	27.9618	40.2370	13.55	265	85	-169	31	23
26	2014184000001	2014.07.03 05:04:46	4.0	27.9380	40.2017	11.92	277	89	-115	43	58
27	2009117000004	2009.04.27 19:03:07	3.8	27.5258	40.7322	15.60	265	62	-144	24	38
28	2016095000000	2016.04.04 16:31:29	3.0	27.5972	40.3520	10.19	300	66	-115	24	18
29	2015355000000	2015.12.21 01:16:00	2.8	27.2780	40.2260	14.95	247	66	112	30	25
30	2014253000008	2014.09.10 22:33:41	2.8	27.5017	40.2963	10.10	92	84	-162	25	23
31	2008197000000	2008.07.15 09:19:49	3.6	27.4393	40.3610	14.82	76	40	179	29	26
32	2010149000000	2010.05.29 02:05:58	2.8	27.4297	40.5865	14.48	308	86	167	27	29
33	2010365000002	2010.12.31 20:57:37	3.7	27.3632	40.5658	15.28	254	55	-165	29	31
34	2016088000007	2016.03.28 17:23:47	3.2	27.5182	40.7303	14.21	247	89	161	22	27
35	2014281000001	2014.10.08 03:08:50	2.9	27.4715	40.7865	17.42	277	30	-176	24	24
36	2009024000007	2009.01.24 15:58:40	3.9	27.7547	40.7892	14.90	149	32	-108	27	44
37	2010299000004	2010.10.26 22:09:41	3.2	27.6792	40.8008	10.78	265	57	119	14	30
38	2013289000001	2013.10.16 12:53:43	2.8	27.6767	40.8080	18.40	86	83	-172	31	26
39	2011206000020	2011.07.25 20:43:53	3.3	27.7490	40.7978	9.38	253	53	-175	28	29
40	2009077000008	2009.03.18 16:33:38	3.4	27.7420	40.8058	9.40	261	63	176	27	39
41	2015301000001	2015.10.28 16:20:03	3.9	27.7495	40.8122	11.79	308	39	-86	43	39
42	2011206000001	2011.07.25 17:57:21	4.5	27.7508	40.8132	11.90	278	48	-103	37	43
43	2009025000009	2009.01.25 08:28:38	2.7	27.7552	40.7995	12.66	85	78	-93	29	24
44	2009023000001	2009.01.23 16:34:52	3.3	27.7572	40.7953	13.26	156	36	-101	25	42
45	2009025000002	2009.01.25 02:54:23	2.8	27.7582	40.7945	12.25	88	47	-122	30	33
46	2012159000003	2012.06.07 20:54:26	4.3	27.9180	40.8402	11.55	98	56	-156	24	34

B. Focal mechanisms and underlying first-motions

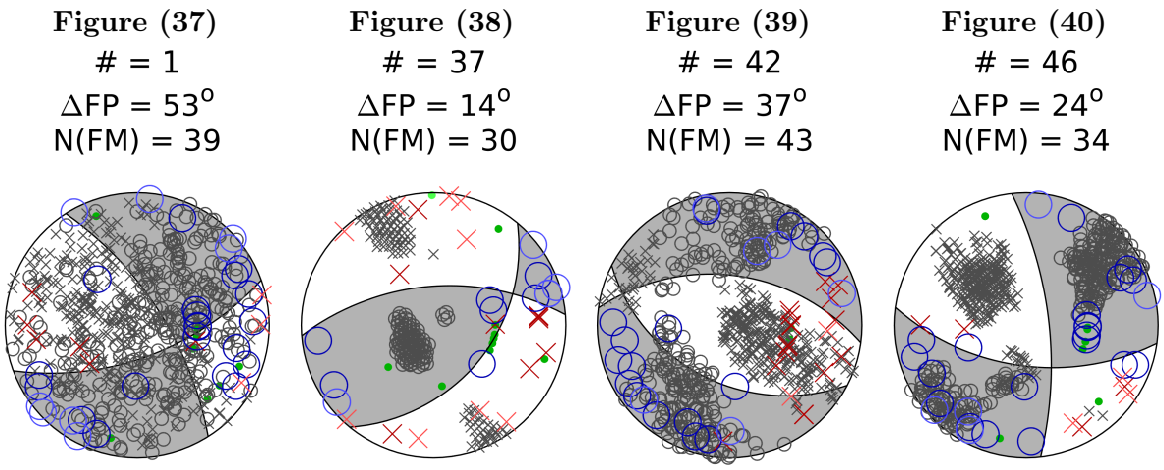

Figure 40: Four exemplary focal mechanism solutions from Fig. 34 and Table 5. Inverted first-motion polarities are shown as blue circles, red crosses and green dots resembling up, down and indeterminable first motions, respectively. The P- and T-axis of "acceptable solutions" returned by HASH [Hardebeck and Shearer, 2002] are shown as gray circles and crosses, respectively. The title lists the focal mechanism ID (#), focal plane uncertainty (ΔFP) and number of first-motions inverted (N(FM)).

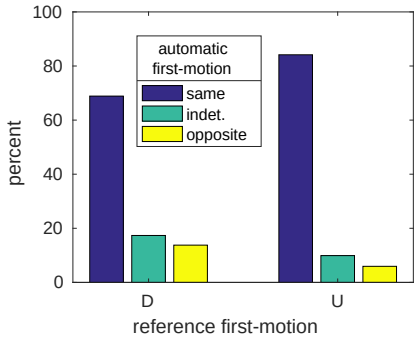

Figure 41: Automatically calculated first-motions in relation to previously manually determined Up- and Down-first-motions.

C. Flip-book of initial, new absolute and new relocated hypocenter locations

We compared the original to our new absolute locations as well as the latter to the relative relocations with respect to the epicentral as well as the depth distribution in the cross-sections shown along the Marmara Section, the Southern Shelf Margin and the Princes' Island segment by plotting dislocation vectors in Fig. 23 and 25. Although this is the most concise way to compare two catalogues, many of the dislocation vectors overlap thus obscuring some of the details. We here plot the catalogues individually each on a new page, in order to compare old and new locations in a flip-book like manner. The catalogues are organized as follows:

1. Merged catalogue (original locations, Fig. 43)
2. Fair absolute locations (Fig. 45)
3. Absolute locations (restricted to corresponding relative relocation, Fig. 47)
4. Relative relocations (Fig. 49)
5. Merged catalogue (restricted to corresponding relative relocation, Fig. 51)

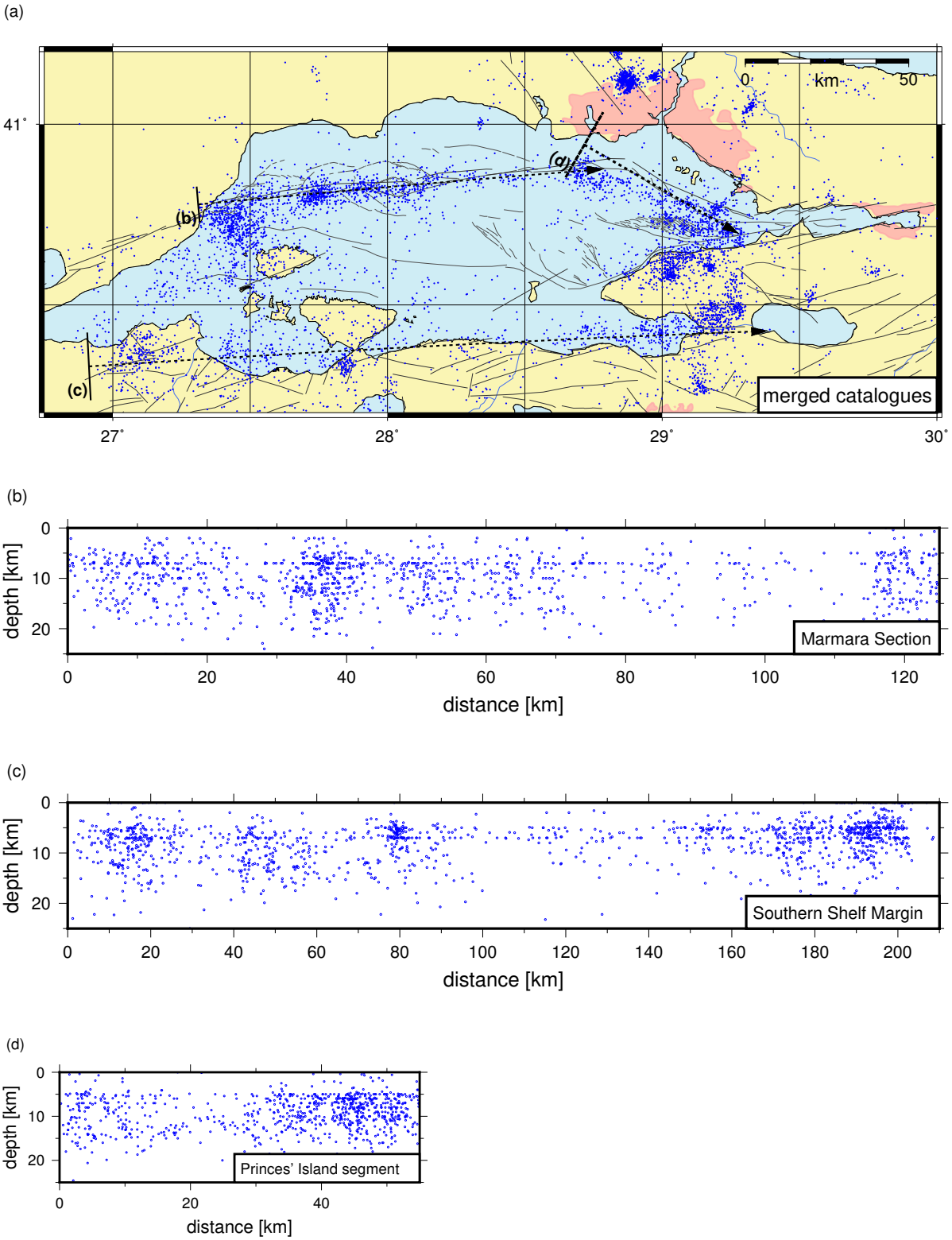

Figure 43: Merged original catalogues (restricted to events with a correspondent in the catalogue of fair absolute locations).

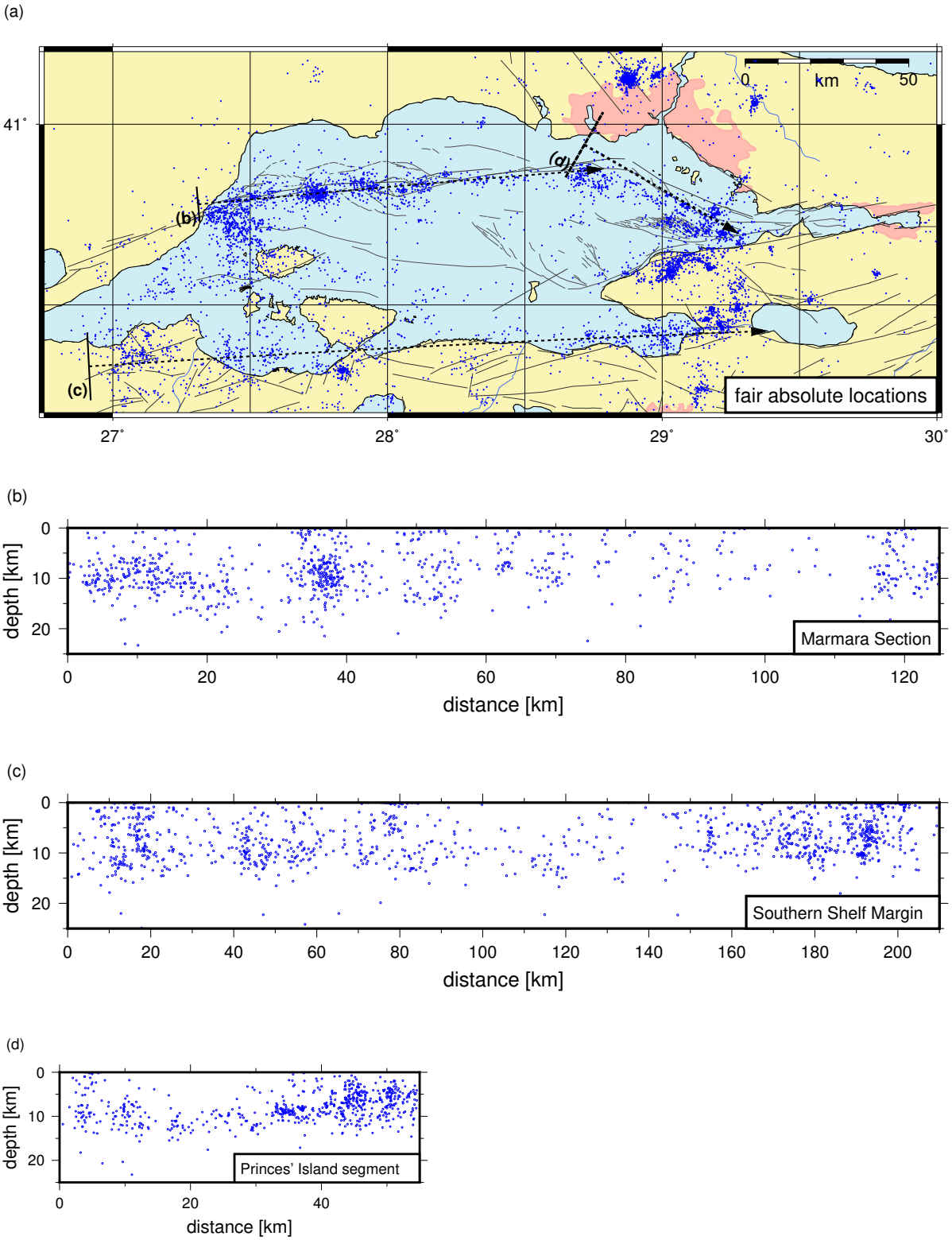

Figure 45: Fair absolute locations.

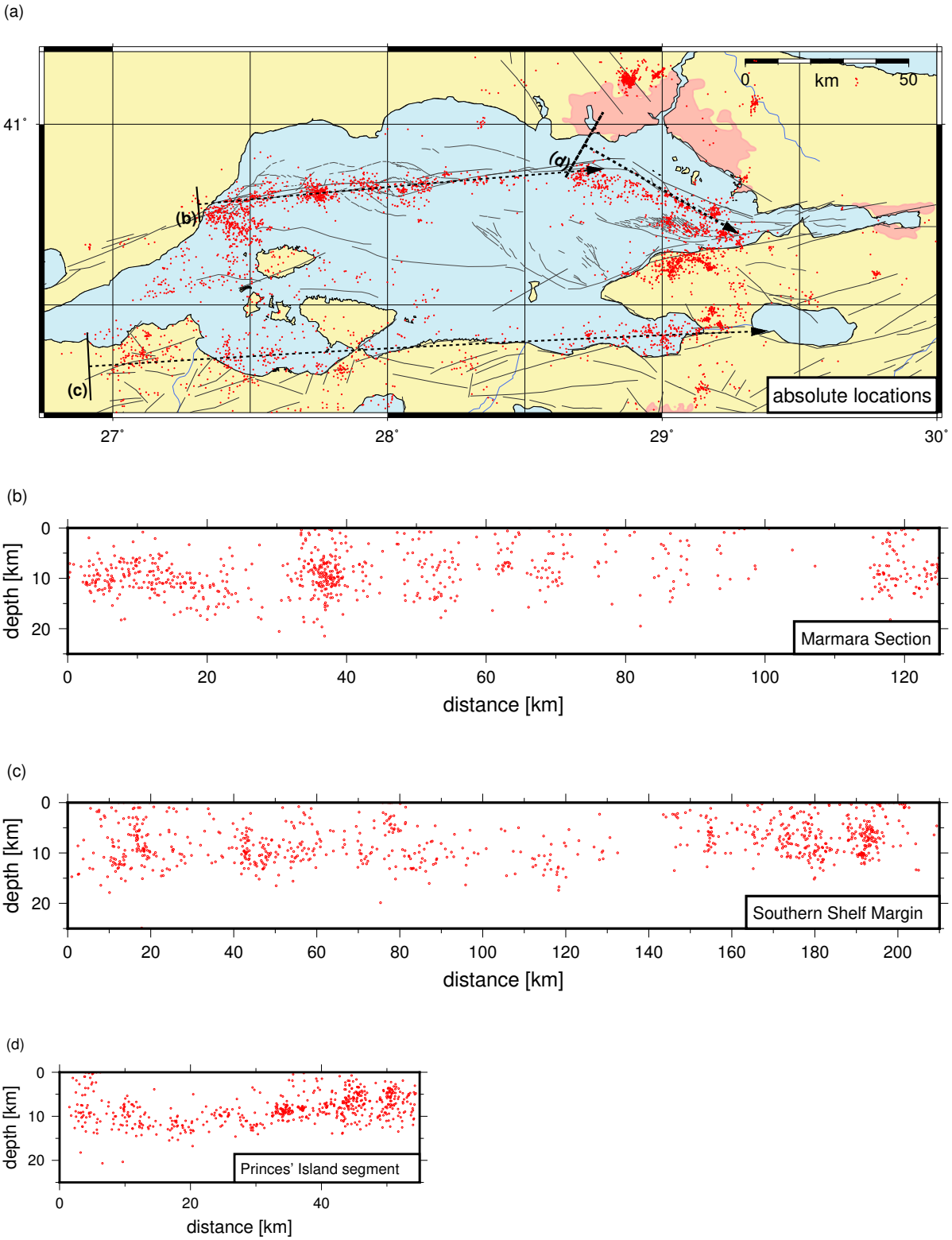

Figure 47: Fair absolute locations (restricted to events with a correspondent in the catalogue of the very best relocations).

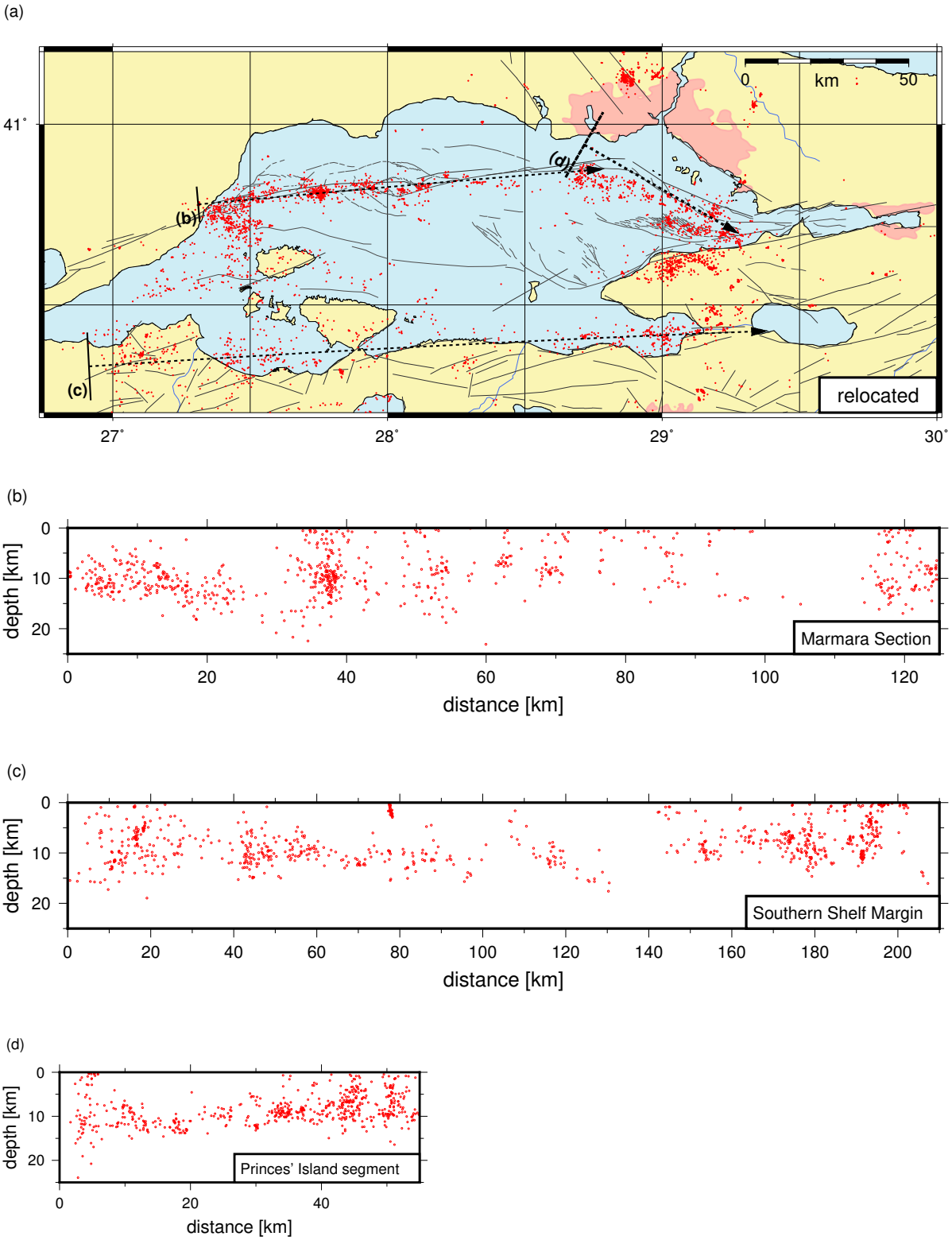

Figure 49: Relocated catalog.

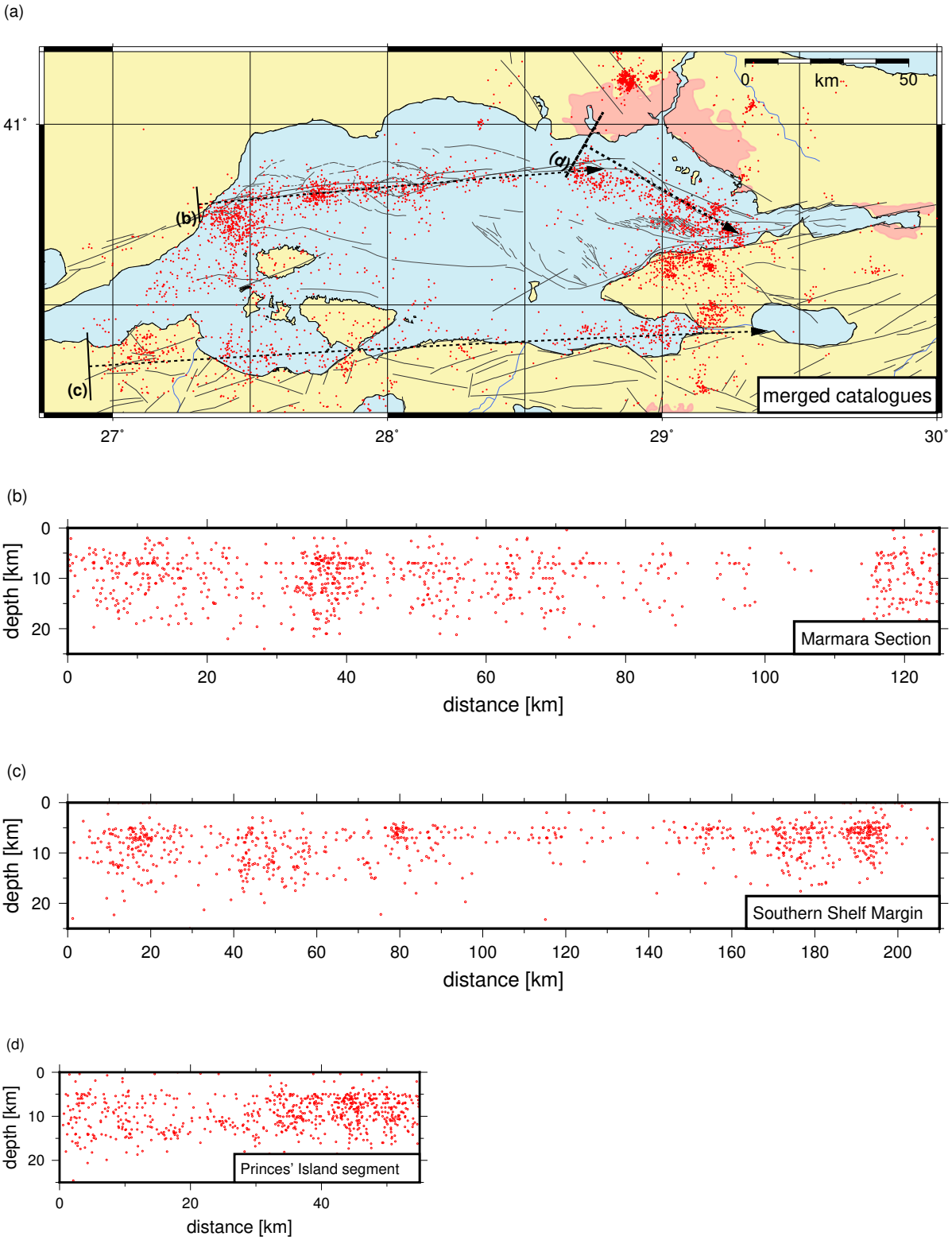

Figure 51: Merged original catalogues (restricted to events with a correspondent in the catalogue of the very best relocations).